Light Dirac neutrino portal dark matter with gauged $U(1)_{B-L}$ symmetry

Nayan Das* and Debasish Borah†

Department of Physics, Indian Institute of Technology Guwahati, Assam 781039, India

(Received 17 January 2024; accepted 8 April 2024; published 29 April 2024)

We propose a gauged $U(1)_{B-L}$ version of the light Dirac neutrino portal dark matter. The $U(1)_{B-L}$ symmetry provides a UV completion by naturally accommodating three right-handed neutrinos from anomaly cancellation requirements which, in combination with the left-handed neutrinos, form the sub-eV Dirac neutrinos after electroweak symmetry breaking. The particle content and the gauge charges are chosen in such a way that light neutrinos remain purely Dirac and dark matter, a gauge singlet Dirac fermion, remain stable. We consider both thermal and nonthermal production possibilities of dark matter and correlate the corresponding parameter space with the one within reach of future cosmic microwave background (CMB) experiments sensitive to enhanced relativistic degrees of freedom $\Delta N_{\rm eff}$. The interplay of dark matter, CMB, structure formation and other terrestrial constraints keep the scenario very predictive leading the $U(1)_{B-L}$ parameter space into tight corners.

DOI: 10.1103/PhysRevD.109.075045

I. INTRODUCTION

The observations of dark matter (DM) in astrophysics and cosmology related experiments together with nonzero neutrino mass and mixing provide strong evidence for beyond standard model (BSM) physics [1,2]. Just like the particle nature of DM is not yet known, there are several unknowns in neutrino physics, including the origin of neutrino mass. The nature of neutrinos: Dirac or Majorana, is one of them. While there exist several BSM proposals for particle DM, the weakly interacting massive particle (WIMP) and feebly interacting massive particle (FIMP) scenarios have been studied extensively in the literature. In a typical WIMP scenario,[1] a particle DM candidate having mass and interaction strength with standard model (SM) particles typically around the electroweak ballpark can give rise to the observed DM abundance after thermal freeze-out. On the other hand, in FIMP paradigm,[2] the DM can never enter equilibrium with the SM bath in the early universe due to its feeble interactions with the latter. Such a DM candidate, with negligible initial abundance, freezes in by virtue of decay or scattering from other particles in the bath.

In this work, we consider a scenario where the origin of DM is related to the Dirac nature of light neutrinos, known as the light Dirac neutrino portal DM [5,6] scenario.[3] In such a setup, light Dirac neutrinos take the role of mediating the interactions between DM and the SM bath. In [5] and [6], the DM was assumed to be of WIMP and FIMP type respectively. In addition to linking the origin of neutrino mass and nature with DM, this also offers additional discovery prospects due to right chiral part of Dirac neutrinos, contributing to the effective relativistic degrees of freedom $N_{\rm eff}$. Measurement related to the cosmic microwave background (CMB) puts tight constraints $N_{\rm eff} = 2.99^{+0.34}_{-0.33}$ at 2σ or 95% CL including baryon acoustic oscillation (BAO) data [19]. Similar bound also exists from big bang nucleosynthesis (BBN) $2.3 < N_{\rm eff} < 3.4$ at 95% CL [20]. Both of these cosmological bounds are consistent with the SM predictions $N^{\rm SM}_{\rm eff} = 3.045$ [21–23].[4] Future CMB experiment CMB Stage IV (CMB-S4) is expected reach a much better sensitivity of $\Delta N_{\rm eff} = N_{\rm eff} - N^{\rm SM}_{\rm eff} = 0.06$ [25], taking it closer to the SM prediction. Thus, Dirac neutrino scenarios can be probed in future CMB experiments if right-handed neutrinos (RHN) can be sufficiently produced in the early universe via thermal or nonthermal processes. Light Dirac neutrino models often lead to enhanced $\Delta N_{\rm eff}$, some recent works on which can be found in [5,26–43]. In earlier works

*nayan.das@iitg.ac.in
†dborah@iitg.ac.in

[1]A recent review of WIMP type scenarios can be found in [3].

[2]A recent review of FIMP can be found in [4].

[3]Neutrino portal DM has been studied in several earlier works where either SM light neutrino or heavy neutrinos were considered as the portal [7–18].

[4]A very recent paper [24] reports $N^{\rm SM}_{\rm eff} = 3.043$ by incorporating next-to-leading order correction to $e^+e^- \leftrightarrow \nu_L\bar{\nu}_L$ interactions along with finite temperature QED corrections to the electromagnetic plasma density and effect of neutrino oscillations.

on light Dirac neutrino portal DM, discrete symmetry like Z_4 was considered to get the desired couplings, mass terms as well as the stability of DM. Here, we consider a UV completion with a gauged $B-L$ framework. The right-handed neutrinos are naturally part of the model providing the minimal anomaly-free setup. While RHNs are thermally produced due to gauged $B-L$ interactions, DM can be of WIMP or FIMP type depending upon Dirac neutrino portal couplings. The model not only gives rise to the desired DM phenomenology with observable $\Delta N_{\rm eff}$, but also leads to new constraints in the gauged $B-L$ parameter space not obtained previously.

This paper is organized as follows. In Sec. II, we briefly discuss the minimal gauged $U(1)_{B-L}$ model of light Dirac neutrino portal dark matter followed by separate discussions of FIMP and WIMP type DM in Secs. III and IV, respectively. We finally conclude in Sec. V.

II. THE MODEL

Gauged $B-L$ extension of the SM [44–49] has been a popular BSM framework studied in the context of neutrino mass among others. The three right-handed neutrinos ν_R having $B-L$ charge -1 each not only keep the model anomaly free[5] but also lead to massive Dirac neutrinos in combination with ν_L after electroweak symmetry breaking. A singlet fermion ψ is considered to be the DM candidate while two singlet scalars ϕ_1 and ϕ_2 with nonzero $B-L$ charges help in realizing light Dirac neutrino portal DM and spontaneous $B-L$ symmetry breaking respectively. The relevant particle content is shown in Table I.

The scalar Lagrangian for the model can be written as

$$\mathcal{L}_{\rm s} = (D^\mu\Phi)^\dagger D_\mu\Phi + (D^\mu\phi_1)^\dagger D_\mu\phi_1 + (D^\mu\phi_2)^\dagger D_\mu\phi_2 - V(\Phi,\phi_1,\phi_2), \tag{1}$$

where

$$D_\mu\Phi = \left(\partial_\mu - i\frac{g}{2}\tau_a W_\mu^a - i\frac{g'}{2}B_\mu\right)\Phi,$$
$$D_\mu\phi_1 = (\partial_\mu - ig_{BL}B'_\mu)\phi_1, \quad D_\mu\phi_2 = (\partial_\mu - i3g_{BL}B'_\mu)\phi_2, \tag{2}$$

denote the respective covariant derivatives and

$$\begin{aligned} V(\Phi,\phi_1,\phi_2) = {} & -\mu^2(\Phi^\dagger\Phi) + \mu_1^2(\phi_1^\dagger\phi_1) - \mu_2^2(\phi_2^\dagger\phi_2) \\ & + \lambda(\Phi^\dagger\Phi)^2 + \lambda_1(\phi_1^\dagger\phi_1)^2 + \lambda_2(\phi_2^\dagger\phi_2)^2 \\ & + \lambda_{H\phi_1}(\Phi^\dagger\Phi)(\phi_1^\dagger\phi_1) + \lambda_{H\phi_2}(\Phi^\dagger\Phi)(\phi_2^\dagger\phi_2) \\ & + \lambda_{\phi_1\phi_2}(\phi_1^\dagger\phi_1)(\phi_2^\dagger\phi_2) + (\lambda'_{\phi_1\phi_2}\phi_1^3\phi_2^\dagger + \text{H.c.}) \end{aligned} \tag{3}$$

[5]See appendix A for other solutions to anomaly cancellation conditions.

TABLE I. Relevant particle content of the model with respective quantum numbers under the symmetry group.

	L	Φ	ν_R	ψ	ϕ_1	ϕ_2
$SU(2)$	2	2	1	1	1	1
$U(1)_Y$	$-\frac{1}{2}$	$\frac{1}{2}$	0	0	0	0
$U(1)_{B-L}$	-1	0	-1	0	1	3

denotes the scalar potential. The relevant part of the fermion Lagrangian is

$$-\mathcal{L}_{\rm Y} \supset Y_\nu \bar{L}\tilde{\Phi}\nu_R + y_{\phi_1}\bar{\psi}\phi_1\nu_R + m_\psi\bar{\psi}\psi. \tag{4}$$

The singlet scalar field ϕ_2 acquires a nonzero vacuum expectation value (VEV) denoted by $\langle\phi_2\rangle = v_2$, leading to the spontaneous breaking of $U(1)_{B-L}$ gauge symmetry. The singlet field ϕ_1 does not acquire any VEV and remains heavier than DM ψ, ensuring latter's stability. We also consider the Higgs portal coupling $\lambda_{H\phi_2}$ to be negligible for simplicity.

Considering the free parameters in the model to be μ_1, $\mu_2, \lambda_1, \lambda_2, \lambda_{H\phi_1}, \lambda'_{\phi_1\phi_2}, g_{BL}, y_{\phi_1}, m_\psi$, the physical masses of ϕ_1, ϕ_2 and Z' (the $U(1)_{B-L}$ gauge boson) can be written as

$$m_{\phi_1}^2 = \mu_1^2 + \frac{1}{2}\lambda_{H\phi_1}v^2, \tag{5}$$

$$m_{\phi_2}^2 = 2\lambda_2 v_2^2, \tag{6}$$

$$m_{Z'}^2 = 9g_{B-L}^2 v_2^2, \tag{7}$$

where $v\left(=\sqrt{\frac{\mu^2}{\lambda}}\right)$ and $v_2\left(=\sqrt{\frac{\mu_2^2}{\lambda_2}}\right)$ are the VEVs of the neutral component of the SM Higgs Φ and ϕ_2 respectively. As a result, the parameters μ_1, μ_2, and λ_2 can be traded for the parameters m_{ϕ_1}, m_{ϕ_2}, and $m_{Z'}$. This leads to the free parameters as $m_{\phi_1}, m_{\phi_2}, m_{Z'}, \lambda_1, \lambda_{H\phi_1}, \lambda'_{\phi_1\phi_2}, g_{BL}, y_{\phi_1}, m_\psi$, out of which the relevant parameters for the phenomenology to be discussed are[6] $m_{\phi_1}, m_{Z'}, m_\psi, \lambda_{H\phi_1}, g_{BL}, y_{\phi_1}$.

While we have a gauged $B-L$ symmetry, DM is neutral under $U(1)_{B-L}$ and its relic depends on the Dirac neutrino portal couplings in the spirit of light Dirac neutrino portal DM [5,6]. Now, depending on the value of this Dirac neutrino portal Yukawa coupling y_{ϕ_1}, the DM analysis can be broadly divided into two categories namely, (a) FIMP ($y_{\phi_1} < 10^{-7}$) and (b) WIMP ($y_{\phi_1} > 10^{-7}$). In the first case, due to small Yukawa coupling, the DM ψ is produced nonthermally and dominantly from ϕ_1 decay. In the second case, DM can attain equilibrium in the early universe due to

[6]The scalar ϕ_2 is not expected to play any role in dark matter analysis. First of all, DM does not couple directly to ϕ_2. Also, ϕ_2 is heavier than the rest of the particles and hence does not appear in final states.

sizeable interactions. We now discuss these two broad cases one by one.

III. FIMP TYPE DARK MATTER

In this scenario, the Yukawa coupling among ν_R, DM and singlet scalar is small $y_{\phi_1} < 10^{-7}$ keeping the associated processes out-of-equilibrium throughout. While DM never thermalizes, the RHNs can thermalize with the SM bath by virtue of $U(1)_{B-L}$ gauge interactions. Similar to the active neutrinos, the RHNs also contributes to the effective relativistic degrees of freedom defined as

$$N_{\rm eff} \equiv \frac{8}{7}\left(\frac{11}{4}\right)^{4/3}\left(\frac{\rho_{\rm rad}-\rho_\gamma}{\rho_\gamma}\right), \tag{8}$$

where $\rho_{\rm rad}$ is the net radiation content of the universe.[7] As mentioned earlier, the SM prediction is $N_{\rm eff}^{\rm SM} = 3.045$ [21–23]. In our model for thermal right-handed neutrinos (ν_R), $\Delta N_{\rm eff}$ can be estimated by finding the decoupling temperature T_{ν_R} of ν_R using

$$\Gamma(T_{\nu_R}) = \mathcal{H}(T_{\nu_R}) \tag{9}$$

where $\Gamma(T)$ is the interaction rate and $\mathcal{H}(T)$ is the expansion rate of the universe.

Let us consider the thermalization of ν_R with the SM bath via the Z' portal interactions. Sufficiently large Z' portal interactions can lead to thermalization of ν_R via the s-channel process $f\bar{f} \leftrightarrow \nu_R\bar{\nu}_R$ (here f denotes SM fermions). As a result, ν_R enters the thermal bath and then, after a certain period, it decouples from the bath. This generates the thermal contribution of ν_R to $\Delta N_{\rm eff}$ [26]. Fig. 1 shows the thermal $\Delta N_{\rm eff}$ as a function of coupling g_{BL} and gauge boson mass $m_{Z'}$. Thus for $g_{BL} \gtrsim 10^{-8}$, $\Delta N_{\rm eff}$ receives a thermal contribution from light Dirac neutrinos which we denote as $\Delta N_{\rm eff}^{\rm th}$. The region corresponding to large Z' portal interactions, labeled as $\Delta N_{\rm eff} > 0.28$ is disfavored by Planck 2018 limits at 2σ CL

On the other hand, due to the tiny dark sector Yukawa coupling y_{ϕ_1}, it is also possible to get a nonthermal contribution to $\Delta N_{\rm eff}$ [6,33], which we denote by $\Delta N_{\rm eff}^{\rm non-th}$. In addition to the Yukawa coupling y_{ϕ_1} involved in $\phi_1 - \nu_R - \psi$ coupling, the $U(1)_{B-L}$ portal coupling and scalar portal coupling $\lambda_{H\phi_1}$ can also play a crucial role in deciding the strength of this nonthermal contribution. While the total contribution to $\Delta N_{\rm eff}$, in general, is a

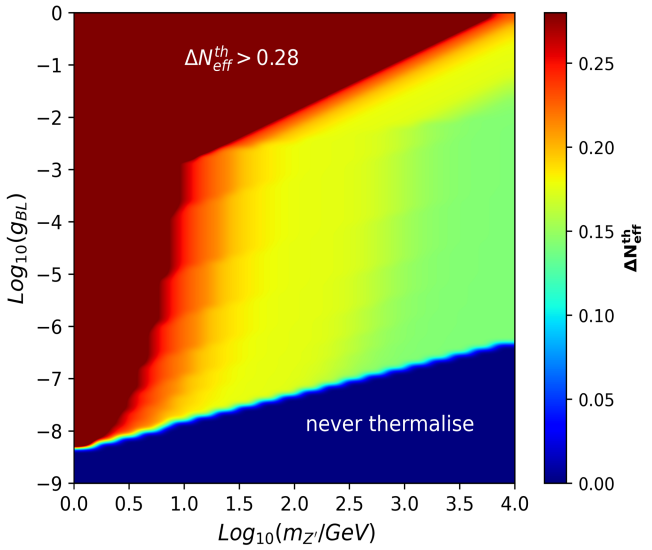

FIG. 1. $\Delta N_{\rm eff}^{\rm th}$ as a function of $m_{Z'}$ and g_{BL}.

combination of thermal contribution and nonthermal contribution, the latter can occur only if the decoupling of RHNs precedes the nonthermal or freeze-in production.

To study this nonthermal contribution $\Delta N_{\rm eff}^{\rm non-th}$ in details, let us first consider the situation where ϕ_1 remains in thermal equilibrium initially and then freezes out from the bath. The frozen out ϕ_1 later decays into ψ and ν_R, leading to nonthermal production of both dark matter and ν_R. The nonthermal contribution to $\Delta N_{\rm eff}$ from ν_R can be calculated from the total energy density of frozen-in Dirac neutrinos.

The Boltzmann equation for comoving number density of ϕ_1 can be written as

$$\frac{dY_{\phi_1}}{dx} = \frac{\beta s}{\mathcal{H}x}\left(-\langle\sigma v\rangle_{\phi_1\phi_1^\dagger\to X\bar{X}}((Y_{\phi_1})^2 - (Y_{\phi_1}^{\rm eq})^2) - \frac{\Gamma_{\phi_1}}{s}\frac{K_1(x)}{K_2(x)}Y_{\phi_1}\right), \tag{10}$$

where K_1 and K_2 are the modified Bessel functions of first and second kind respectively. The comoving abundance of species i is defined as $Y_i = n_i/s$ with n_i, s being number density of species i and entropy density of the universe respectively. $\mathcal{H}$ denotes the Hubble parameter. The variable x is defined as $x = m_{\phi_1}/T$ and $\beta = 1 + \frac{T}{3g_*^s}\frac{dg_*^s}{dT}$ with g_*^s being the relativistic entropy degrees of freedom. Here $\langle\sigma v\rangle_{\phi_1\phi_1^\dagger\to X\bar{X}}$ is the thermally averaged annihilation cross section of ϕ_1 into the all allowed final state particles and Γ_{ϕ_1} denotes the decay rate of ϕ_1 into ν_R and ψ. The annihilation cross section of ϕ_1 depends upon Higgs portal coupling $\lambda_{H\phi_1}$ as well as $U(1)_{B-L}$ portal coupling. Depending upon the strength of these individual couplings, the freeze-out abundance of ϕ_1 is either determined by scalar portal or gauge portal interactions. The freeze-in

[7]Due to the presence of three relativistic RHNs, change in $N_{\rm eff}$ can be written as $\Delta N_{\rm eff} = 3\frac{\rho_{\nu_R}}{\rho_{\nu_L}}\Big|_{\rm CMB} = 3\frac{\rho_{\nu_R}}{\rho_{\nu_L}}\Big|_{10\ \rm MeV} = 3\left(\frac{T_{\nu_R}}{T_{\nu_L}}\right)^4\Big|_{10\ \rm MeV}$. Here ρ_{ν_L} denotes energy density of one species of SM neutrinos. For nonthermal RHNs, ρ_{ν_R} should be calculated by solving appropriate Boltzmann equation whereas for thermal RHNs, ρ_{ν_R} can be written in terms of its decoupling temperature.

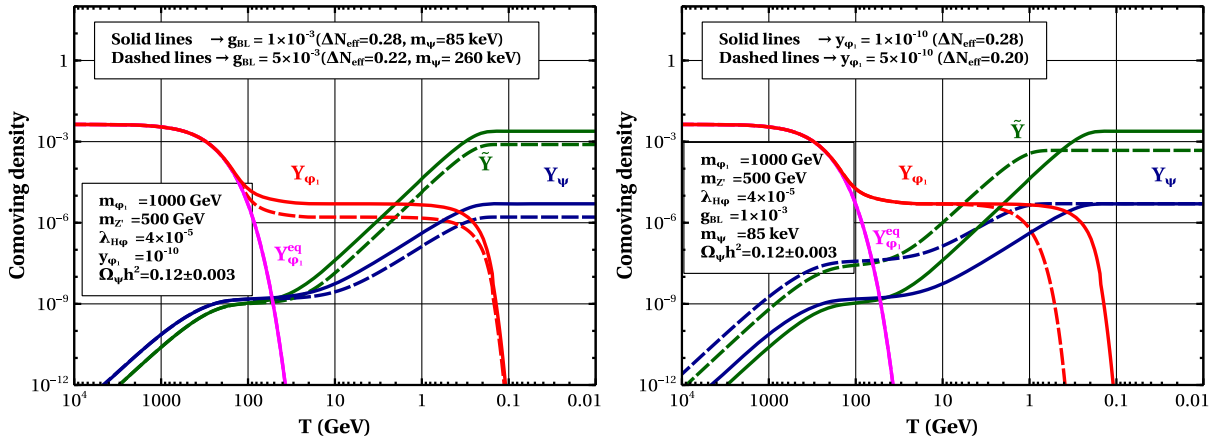

FIG. 2. Evolution of comoving number density of ϕ_1, ψ and comoving energy density of ν_R. The left (right) panel shows the variation with respect to g_{BL} (y_{ϕ_1}).

abundance of ψ and ν_R (from the decay of frozen out ϕ_1) can be obtained by solving the relevant Boltzmann equations given by

$$\frac{dY_\psi}{dx} = \frac{\beta}{x\mathcal{H}}\Gamma_{\phi_1}\frac{K_1(x)}{K_2(x)}Y_{\phi_1}, \tag{11}$$

$$\frac{d\tilde{Y}}{dx} = \frac{\beta}{\mathcal{H}s^{1/3}x}\langle E\Gamma\rangle_{\phi_1}Y_{\phi_1}, \tag{12}$$

with

$$\Gamma_{\phi_1} = \frac{1}{32\pi}m_{\phi_1}y^2_{\phi_1}\left(1-\frac{m^2_\psi}{m^2_{\phi_1}}\right)^2;$$
$$\langle E\Gamma\rangle_{\phi_1} = \frac{1}{64\pi}m^2_{\phi_1}y^2_{\phi_1}\left(1-\frac{m^2_\psi}{m^2_{\phi_1}}\right)^3.$$

The term $\tilde{Y} = \frac{\rho_{\nu_R}}{s}$ represents the comoving energy density of RHNs. The preferred choice of energy density instead of number density of ν_R is based on the fact that the calculation of $\Delta N_{\rm eff}$ requires comoving energy density of ν_R.

The nonthermal contribution to $\Delta N_{\rm eff}$ namely, $\Delta N^{\rm non-th}_{\rm eff}$ depends on the parameters $m_{\phi_1}, m_{Z'}, \lambda_{H\phi_1}, g_{BL}$ and y_{ϕ_1}. While the parameters $m_{\phi_1}, m_{Z'}, \lambda_{H\phi_1}$ and g_{BL} determine the freeze-out abundance of ϕ_1, the parameters that determine the decay width of ϕ_1 are m_{ϕ_1}, y_{ϕ_1}. Fig. 2 shows the evolution of comoving densities for chosen benchmark points clearly indicating the roles of g_{BL} and y_{ϕ_1}. While we only show the evolution of nonthermal contribution to $\Delta N_{\rm eff}$ in this figure, the total $\Delta N_{\rm eff}$ for the chosen benchmark values of parameters include both thermal and nonthermal contributions. In the left panel plot of Fig. 2, the solid line for $\tilde{Y}$ corresponds to an asymptotic nonthermal contribution $\Delta N^{\rm non-th}_{\rm eff} = 0.10$ while the same choice of parameters generates a thermal contribution $\Delta N^{\rm th}_{\rm eff} = 0.18$. Therefore, the total contribution of $\Delta N_{\rm eff} = 0.28$, as indicated in the legends for the solid line. For the dashed line, corresponding to a larger value of g_{BL}, the thermal contribution also comes out to be slightly larger $\Delta N^{\rm th}_{\rm eff} = 0.19$, as expected. However, a significant decrease in nonthermal contribution is observed for this benchmark point leading to $\Delta N^{\rm non-th}_{\rm eff} = 0.03$. Thus, for the dashed line in left panel plot of Fig. 2, we have total $\Delta N_{\rm eff} = 0.22$. For the right panel plot of the same figure, the thermal contribution remains same $\Delta N^{\rm th}_{\rm eff} = 0.18$ as g_{BL} and $m_{Z'}$ are kept fixed and variation in Yukawa coupling y_{ϕ_1} in the nonthermal ballpark does not alter thermal contribution to $\Delta N_{\rm eff}$. The dashed line, with a larger y_{ϕ_1}, have a smaller $\Delta N^{\rm non-th}_{\rm eff} = 0.02$ and vice versa. As a result, for the dashed line in right panel plot, the total contribution is $\Delta N_{\rm eff} = 0.20$. In both the left and right panel plots, the values of m_ψ are taken in such a way that it gives correct FIMP type dark matter relic. Also, we have seen that the value of m_ψ does not affect $\Delta N_{\rm eff}$ as long as $m_\psi \ll m_{\phi_1}$.

After studying the evolution of comoving densities for different benchmark points, we perform a numerical scan over key model parameters to find out the parameter space consistent with $\Delta N_{\rm eff}$ and DM properties. We have kept m_{ϕ_1} fixed at 1000 GeV and y_{ϕ_1} at 10^{-10}. The rest of the parameters are varied in the following range:

$$\begin{aligned} 250\ \text{GeV} < m_{Z'} < 1000\ \text{GeV} \\ 10^{-5} < \lambda_{H\phi_1} < 5\times10^{-5} \\ 10^{-4} < g_{BL} < 10^{-2} \\ 10^{-5}\ \text{GeV} < m_\psi < 10^{-3}\ \text{GeV}. \end{aligned} \tag{13}$$

The resulting parameter space in terms of $\Delta N_{\rm eff}$ and $m_{Z'}$ is shown in Fig. 3. All the points shown in this figure satisfy the requirements of correct DM relic abundances. The magenta shaded region denotes the region excluded by

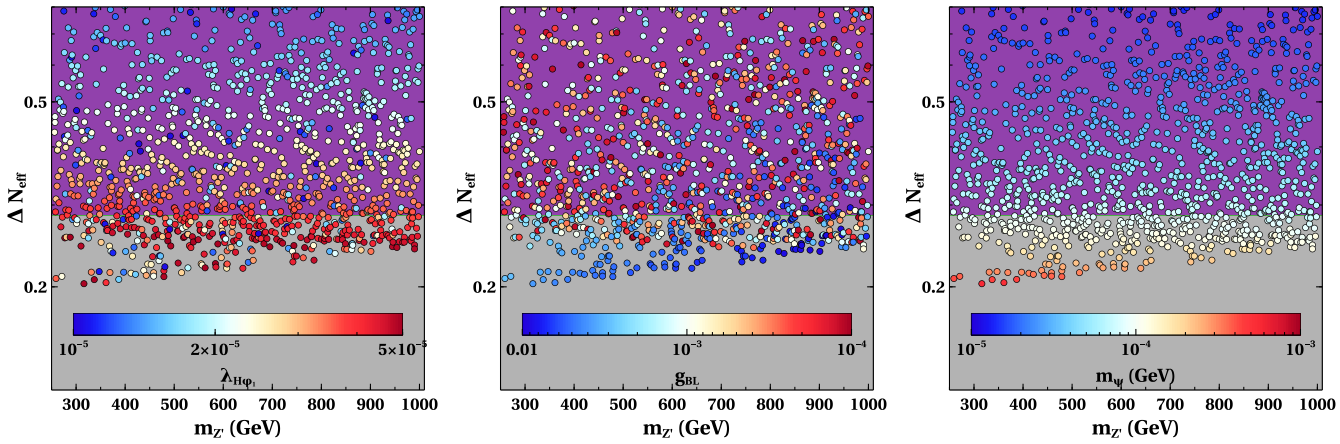

FIG. 3. Scan plot showing the total $\Delta N_{\rm eff}$ versus $m_{Z'}$ for different $\lambda_{H\phi_1}$, g_{BL} and m_ψ. The magenta colored region is excluded by Planck 2018 bounds at 2σ CL The region in gray color is within the reach of future experiments.

Planck 2018 bounds at 2σ CL while the gray shaded region remains within the reach of future experiments like CMB-S4. The color codes in the left, middle, and right panel plots of Fig. 3 show the variation in $\lambda_{H\phi_1}, g_{BL}, m_\psi$ respectively. As the left panel plot shows, decrease in $\lambda_{H\phi_1}$, while keeping m_{ϕ_1} constant, increases $\Delta N_{\rm eff}$. A smaller value of Higgs portal coupling $\lambda_{H\phi_1}$ leads to a larger freeze-out abundance of ϕ_1 followed by enhanced production of ν_R from ϕ_1 decay. Since the same decay is also responsible for freeze-in production of DM, we require smaller DM masses in order to keep its relic abundance within Planck limits, as seen from the right panel plot of Fig. 3. As the middle panel plot shows, small values of $\Delta N_{\rm eff}$ typically correspond to smaller g_{BL} as the corresponding thermal contribution $\Delta N_{\rm eff}^{\rm th}$ decreases.

While we have incorporated the constraints from cosmological observations on $\Delta N_{\rm eff}$ and DM relic abundance, there can be strong constraints on light dark matter from astrophysical structure formation. Such bounds can be imposed on a particular DM scenario by calculating the free-streaming length (FSL) of DM. While hot DM is already ruled out, warm DM with FSL $\lambda_{\rm FSL} < 0.1$ Mpc is still allowed, and can be favorable over cold DM of FSL $\lambda_{\rm FSL} < 0.01$ Mpc due to the small-scale structure problems associated with the latter [50]. Dark matter free-streaming length can be estimated from matter power spectrum inferred from the Lyman-α forest data [51–54] and also from Quasar data [55]. Such estimates are also supported by theoretical and simulation based results [56–59]. For some recent discussions on structure formation constraints on DM production mechanisms, please see [60–62] and references therein. The detailed calculations related to FSL of DM are given in appendix B.

As shown in appendix B, the FSL of DM depends primarily on the production temperature, DM mass and the production mechanism of DM or distribution function of DM. A higher production temperature gives a smaller FSL due to high momentum redshift making DM nonrelativistic earlier and vice-versa. A different production mechanism also gives different FSL. In our case, the DM is produced due to decay of a frozen out scalar. Figure 4 shows the average velocity of DM for four different benchmark parameters. The parameters are shown in Table II along with total $\Delta N_{\rm eff}$ and FSL. The benchmark point (BP) II corresponds to a smaller ϕ_1 mass than BP I. Hence, the freeze-out abundance of ϕ_1 for BP II is smaller than that of BP I. This implies that a larger ψ mass is required to satisfy DM abundance. As a result, we obtain a smaller FSL for BP II. However, for both BP I and BP II, the computed FSL keeps DM in hot DM category and hence ruled out from structure formation constraints. The FSL can be reduced by increasing the production temperature as well as increasing DM mass. BP III and BP IV have a larger y_{ϕ_1} giving a higher production temperature. Similarly it has a larger $\lambda_{H\phi_1}$ coupling, giving smaller ϕ_1 freeze-out abundance.

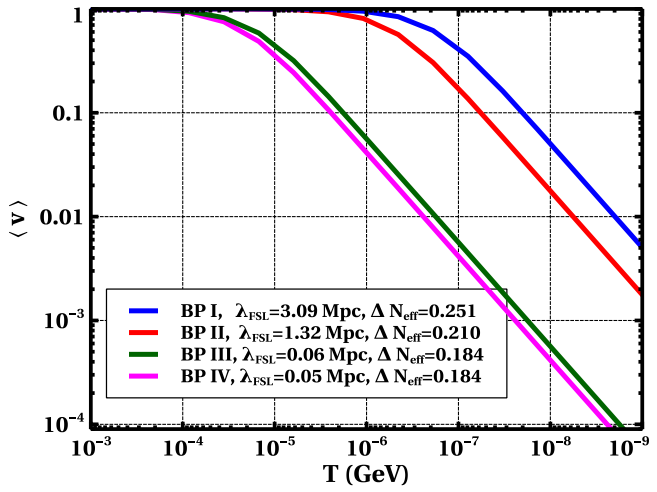

FIG. 4. Thermal average velocity of FIMP dark matter as a function of temperature for four different benchmark points.

TABLE II. Benchmark parameters for FIMP DM.

	Parameters								
	m_{ϕ_1} (GeV)	$\lambda_{H\phi_1}$	y_{ϕ_1}	$m_{Z'}$ (GeV)	g_{BL}	m_ψ (keV)	$\Omega_{\rm DM}h^2$	$\Delta N_{\rm eff}$	FSL (Mpc)
BP I	1000	5×10^{-5}	10^{-10}	500	0.001	126	0.12	0.251	3.09
BP II	500	5×10^{-5}	10^{-10}	500	0.001	233	0.12	0.210	1.32
BP III	1000	2×10^{-4}	10^{-9}	500	0.001	970	0.12	0.184	0.06
BP IV	500	2×10^{-4}	10^{-9}	500	0.001	938	0.12	0.184	0.05

Hence for both BP III and BP IV, DM masses can be large while being consistent with relic abundance criteria. Combining these two effects, we get warm dark matter for BP III and BP IV. From the resulting on $\Delta N_{\rm eff}$, it can be seen that both BP III and BP IV remain within the sensitivity of future CMB experiments like CMB-S4.

Fig. 5 shows the parameter space in $m_{Z'}$ versus g_{BL} parameter space for the FIMP scenario. The left, middle, and right panel plots correspond to dark matter mass of 400 keV, 500 keV and 1300 keV respectively. The other relevant parameters are fixed as $m_{\phi_1}=500$ GeV, $\lambda_{H\phi_1}=10^{-5}$, $y_{\phi_1}=10^{-9}$. For the region below the solid brown line in each of these plots, $U(1)_{B-L}$-portal coupling does not play any role in FIMP DM production. In that region, the freeze-out abundance of ϕ_1, responsible for DM production, is determined by the Higgs-portal coupling $\lambda_{H\phi_1}$. In other words, the cross section $\langle\sigma v\rangle_{\phi_1\phi_1^\dagger\to SM\overline{SM}}$ dominates over $\langle\sigma v\rangle_{\phi_1\phi_1^\dagger\to ZZ'}$. In the region above the solid brown line, the freeze-out abundance of ϕ_1 is determined by the $U(1)_{B-L}$-portal coupling. The dashed line in the left and middle panel plots, separating the pink and cyan shaded regions, represent the parameter space satisfying correct DM relic for $m_\psi=400$ keV and $m_\psi=500$ keV respectively. However, for DM mass $m_\psi=400$ keV, the free-streaming length turns out to be very large ~0.1 Mpc, keeping it in hot DM ballpark and hence ruled out. In the middle panel plot, due to a higher DM mass $m_\psi=500$ keV, the dashed line corresponds to an intermediate FSL keeping it in the warm DM regime which is still allowed by structure formation constraints. In the region below the dashed line, the freeze-out abundance of ϕ_1 is more than that for the dashed line, leading to a larger FIMP DM abundance $\Omega_{\rm DM}h^2>0.12$, produced from ϕ_1 decay. On the other hand, the region above the dashed line have $\Omega_{\rm DM}h^2<0.12$ due to smaller freeze-out abundance of ϕ_1. This is understood from the fact that a larger $U(1)_{B-L}$-portal interaction leads to smaller freeze-out abundance of ϕ_1 and vice versa. While the total $\Delta N_{\rm eff}$ can have both thermal and nonthermal contributions, for the choice of parameters in Fig. 5, the nonthermal contribution is suppressed compared to the thermal contribution. The magenta solid line corresponds to $\Delta N_{\rm eff}=0.28$. The region above this line has $\Delta N_{\rm eff}>0.28$ and hence ruled out from Planck 2018 limits. In the right panel plot, the dashed line corresponds to relic satisfying region for DM mass $m_\psi=1300$ keV. The region below the dashed line correspond to overabundance like before. However, the region above the dashed line is no longer underabundant, but satisfies the current DM abundance. For this region of parameter space and chosen DM mass, the production of FIMP DM while ϕ_1 is in equilibrium dominates compared to the production after ϕ_1 freeze-out. This can also be understood from the evolution plots shown in Fig. 2.

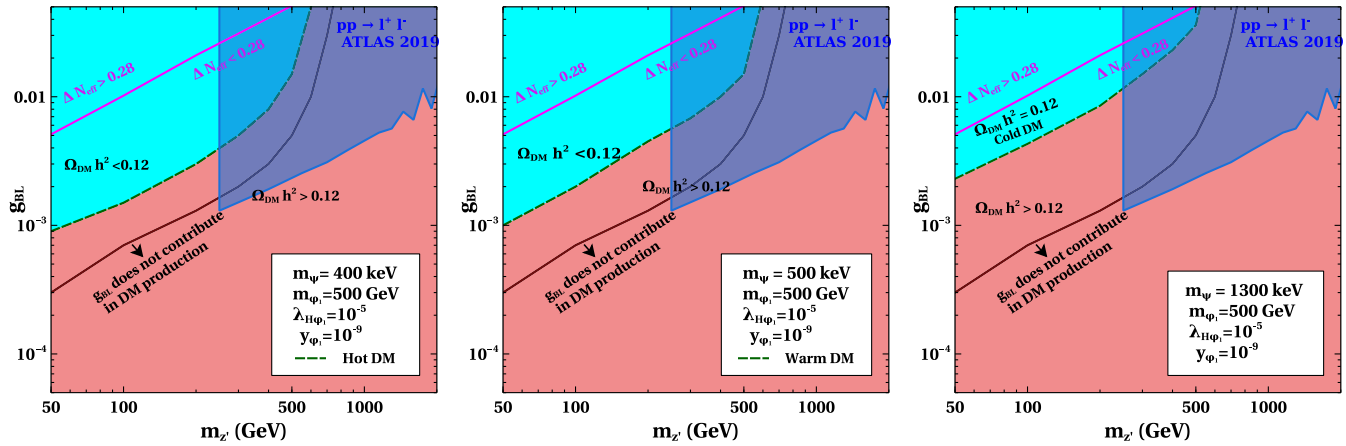

FIG. 5. Parameter space in $m_{Z'}$ versus g_{BL} plane for the FIMP scenario considering three different values of DM mass. The other parameters are kept fixed as $m_{\phi_1}=500$ GeV, $\lambda_{H\phi_1}=10^{-5}$, $y_{\phi_1}=10^{-9}$.

From the left panel plot of Fig. 2, we see that there is a nonzero yield of DM Y_ψ from the decay of ϕ_1 when the latter is in equilibrium. Additionally, the freeze-out abundance of ϕ_1 [$Y_{\phi_1}(x \to \infty)$] decreases as we increase g_{BL}. Combining these two, we can have a situation where for sufficiently large $U(1)_{B-L}$-portal couplings, Y_ψ from the decay of ϕ_1 in equilibrium is larger compared to the post freeze-out production. Hence, $U(1)_{B-L}$-portal couplings do not determine the comoving abundance of Y_ψ and as a result, the region above the dashed line satisfies the correct DM relic in the right panel plot of Fig. 5. In all the plots, the region below the magenta solid line has $0.28 > \Delta N_{\rm eff} > 0.14$ keeping it within reach of future CMB experiments like CMB-S4. The blue shaded region toward the upper right corner indicates the region ruled out from the large hadron collider (LHC) bounds, for specifically from ATLAS experiments at 13 TeV centre of mass energy [63,64]. Similar bounds also exist from the CMS experiment at the LHC [65]. The details of the LHC bound on $g_{BL} - m_{Z'}$ plane is given in appendix C. A relatively weaker bound exists from the large electron positron (LEP) collider disfavoring the region $m_{Z'}/g_{BL} < 7$ TeV [66,67]. The parameter space shown in Fig. 5 already satisfies the LEP bound.

A. When ϕ_1 is always in equilibrium:

Before moving onto the WIMP DM scenario, we briefly comment on the possibility of FIMP DM production from ϕ_1 when the latter remains in equilibrium throughout the production. When ϕ_1 is in equilibrium during the production of DM, the comoving number density of ψ and comoving energy density of ν_R, respectively, are given as

$$\frac{dY_\psi}{dx} = \frac{\beta}{x\mathcal{H}}\Gamma_{\phi_1}\frac{K_1(x)}{K_2(x)}Y^{\rm eq}_{\phi_1}, \tag{14}$$

$$\frac{d\tilde{Y}}{dx} = \frac{\beta}{\mathcal{H}s^{1/3}x}\langle E\Gamma\rangle_{\phi_1}Y^{\rm eq}_{\phi_1}. \tag{15}$$

These two equations can be analytically solved to get the asymptotic abundances (in the limit $m_\psi \ll m_{\phi_1}$)

$$\begin{aligned} Y_\psi(x\to\infty) &= \frac{135}{16\pi\times 1.66\times 8\pi^3 g_*^s\sqrt{g_*^\rho}}M_{\rm pl}\frac{y_{\phi_1}^2}{m_{\phi_1}}, \\ \tilde{Y}(x\to\infty) &= \frac{675}{32\pi\times 1.66\times 8\pi^3 g_*^s\sqrt{g_*^\rho}}\left(\frac{45}{2\pi^2 g_*^s}\right)^{1/3} \\ &\quad\times M_{\rm pl}\frac{y_{\phi_1}^2}{m_{\phi_1}}, \end{aligned} \tag{16}$$

where $M_{\rm pl}$ is the Planck mass. With this, the DM abundance and contribution to extra radiation energy density can be calculated as

$$\begin{aligned} \Omega_{\rm DM}h^2 &= 2\frac{m_\psi s^0}{\rho_c^0}Y_\psi(x\to\infty)h^2 \\ \Delta N_{\rm eff}^{\rm non-th} &= 2\times 3\times\left(\frac{s^{4/3}}{\rho_{\nu_L}}\right)_{\rm T=10\ MeV}\tilde{Y}(x\to\infty) \\ &\simeq 0.61\tilde{Y}(x\to\infty), \end{aligned} \tag{17}$$

where s^0 and ρ_c^0 denote the entropy density and critical energy density, respectively, at the present epoch. ρ_{ν_L} denotes energy density of one species of SM neutrino and h represents $H_0/100$ with H_0 being the current expansion rate of the universe. Here, m_{ϕ_1}, y_{ϕ_1}, and m_ψ determine the DM abundance and $\Delta N_{\rm eff}^{\rm non-th}$ is determined by m_{ϕ_1} and y_{ϕ_1} only. The thermal contribution to $\Delta N_{\rm eff}$ is determined by the parameters $m_{Z'}$ and g_{BL}. When DM abundance is satisfied, it turns out that the nonthermal contribution to $\Delta N_{\rm eff}$ is way below the minimum thermal contribution. So, the total $\Delta N_{\rm eff}$ is only determined by the thermal contribution (shown in Fig. 1).

Fig. 6 shows evolutions of comoving abundances of ϕ_1, ψ and ν_R for two different values of y_{ϕ_1} (left panel) and m_{ϕ_1}

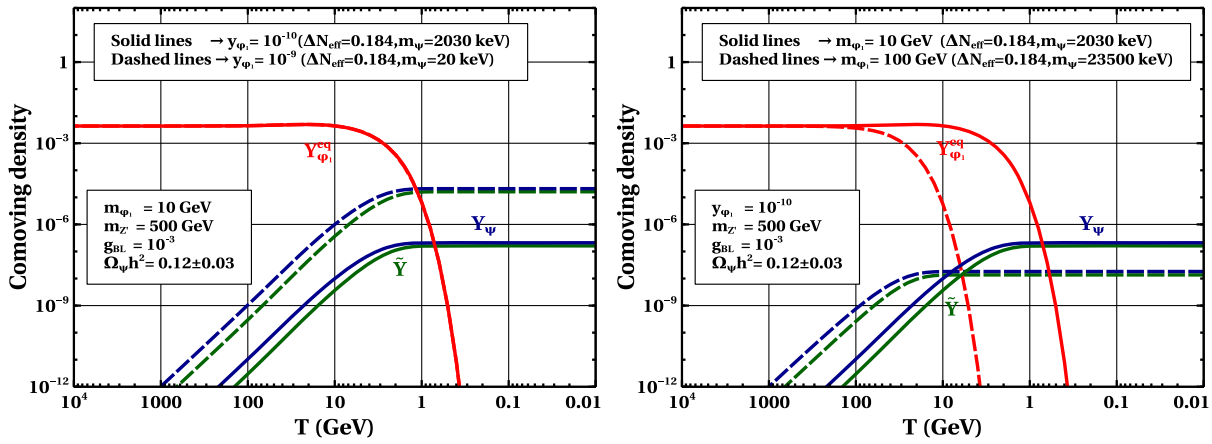

FIG. 6. Evolution of comoving number densities of ϕ_1 and ψ and comoving energy density of ν_R for two different values of y_{ϕ_1} (left panel) and m_{ϕ_1} (right panel).

TABLE III. Table for FIMP DM (equilibrium ϕ_1).

	Parameters							
	m_{ϕ_1} (GeV)	y_{ϕ_1}	$m_{Z'}$ (GeV)	g_{BL}	m_ψ (keV)	$\Omega_{\rm DM}h^2$	$\Delta N_{\rm eff}$	FSL (Mpc)
BP I	10	10^{-10}	500	0.001	2030	0.12	0.184	0.0009
BP II	10	10^{-9}	500	0.001	20	0.12	0.184	0.06
BP III	100	10^{-10}	500	0.001	23500	0.12	0.184	0.0001
BP IV	100	10^{-9}	500	0.001	235	0.12	0.184	0.0064

(right panel). For $m_\psi \ll m_{\phi_1}$ the evolutions for comoving number density of ψ and comoving energy density of ν_R are independent of m_ψ. So in all the evolution plots, the dark matter masses are chosen in such a way that observational DM abundance is satisfied. The solid lines in the left plot have $y_{\phi_1} = 10^{-10}$ and DM mass $m_\psi = 2030$ keV. The nonthermal contribution to $\Delta N_{\rm eff}$ from frozen-in ν_R is 6.5×10^{-6}. For the dashed lines, the Yukawa coupling is larger by a factor of 10. Consequently, we have higher $Y_\psi(x \to \infty)$ and $\tilde{Y}(x \to \infty)$. From Eq. (17), we get DM mass to be 20 keV and $\Delta N_{\rm eff}^{\rm non-th} = 6.5 \times 10^{-4}$. The solid lines in the right plot have the same parameters as those of in the left panel plot. The dashed lines in the right panel plot have $m_{\phi_1} = 100$ GeV. Due to higher mass of ϕ_1, the Boltzmann suppression occurs early on, leading to smaller $Y_\psi(x \to \infty)$ and $\tilde{Y}(x \to \infty)$. As a result DM mass for the solid lines is about 23.5 MeV and $\Delta N_{\rm eff}^{\rm non-th} = 5.5 \times 10^{-7}$. We have kept $B - L$ gauge coupling and mass fixed for all the plots, $g_{BL} = 10^{-3}$ and $m_{Z'} = 500$ GeV. This gives a thermal contribution to $\Delta N_{\rm eff} = 0.184$. As in all the plots nonthermal contribution is way smaller than the thermal counterpart, so the total $\Delta N_{\rm eff}$ is determined by the thermal contribution as shown in the plot. Since $U(1)_{B-L}$-portal parameters do not decide DM abundance in this case, we do not show any summary plot like before.

Table III shows four benchmark points (BP) and their corresponding contribution to effective number of relativistic species and structure formation. BP I and BP II have same $m_{\phi_1} = 10$ GeV whereas BP III and BP IV have $m_{\phi_1} = 100$ GeV. As the Yukawa coupling is ten times larger in BP II compared to BP I, the corresponding DM mass is 100 times smaller in BP II [see Eq. (16)]. The similar trend is followed between BP III and BP IV. Due to smaller DM mass, $\lambda_{\rm FSL}$ is larger in both the BP II (compared to BP I) and BP IV (compared to BP III). Again from Eq. (17), we get that m_{ϕ_1} and m_ψ are correlated for constant DM abundance. Hence a larger m_{ϕ_1} gives a larger m_ψ (BP III, BP IV vs BP I, BP II). The DM production temperature ($T \sim m_{\phi_1}$) is also larger for larger m_{ψ_1}. Combining these two, we get a smaller $\lambda_{\rm FSL}$ for BP III (BP IV) compared to BP I (BP II). Among the four benchmark points mentioned in the table, only BP II gives warm DM whereas rest points give cold DM. As all the points have same $B - L$ gauge coupling and mass, we have same $\Delta N_{\rm eff}$.

IV. WIMP TYPE DARK MATTER

If the Yukawa coupling among the dark sector particles, i.e., ϕ_1, ψ and ν_R is sufficiently strong ($y_{\phi_1} \gg 10^{-7}$), the dark sector can be in thermal equilibrium among themselves even after their decoupling from the SM bath. Since the thermalization of ϕ_1, ν_R with the SM bath relies on Higgs portal and $U(1)_{B-L}$ portal couplings instead of Yukawa y_{ϕ_1}, we have two different subcases depending upon whether the Yukawa interactions in dark sector go out of equilibrium before or after the dark sector decouples from the thermal bath. Among the dark sector particles, ϕ_1 and ν_R can have interactions with other particles in the bath via the processes $\phi_1 X \to \phi_1 X$, $\phi_1 Z' \to \phi_1 Z'$, and $\nu_R X \to \nu_R X$, here X denotes SM particles. Since Z' has sizeable interactions with all the SM fermions, we consider it to be in the bath while dark sector particles decouple. While the first two processes can arise via contact interactions too, the ν_R scattering arises via mediation of heavy Z' boson only. Unlike other interactions, ν_R interactions with the bath rely significantly on resonant enhancement and hence we consider $\nu_R \bar{\nu}_R \to X\bar{X}$ via resonantly enhanced s-channel mediation of Z' to calculate its decoupling [26]. Therefore, the ratio of interaction rate of dark sectors with SM bath to the expansion rate, $\mathcal{H}$, can be written as [68,69]

$$\frac{\Gamma_{\rm total}}{\mathcal{H}} = \frac{1}{\mathcal{H}}[n_X^{\rm eq}(\langle\sigma v\rangle_{\phi_1 X \to \phi_1 X} + \langle\sigma v\rangle_{\phi_1 Z' \to \phi_1 Z'}) + n_{\nu_R}^{\rm eq}\langle\sigma v\rangle_{\nu_R\bar{\nu}_R \to X\bar{X}}]. \tag{18}$$

The decoupling temperature of dark sector is approximately calculated by comparing the total interaction rate with the Hubble expansion rate, i.e., $\frac{\Gamma_{\rm total}}{\mathcal{H}} \approx 1$. Figure 7 shows interaction rates of various processes responsible for keeping the dark sector in bath with the SM as a function of temperature. In the left panel plot, a large scalar portal coupling $\lambda_{H\phi} = 10^{-2}$ dictates the decoupling temperature whereas in the right panel plot, the resonantly enhanced process $\nu_R \bar{\nu}_R \to X\bar{X}$ determines the decoupling temperature due to smaller scalar portal coupling $\lambda_{H\phi} = 10^{-4}$.

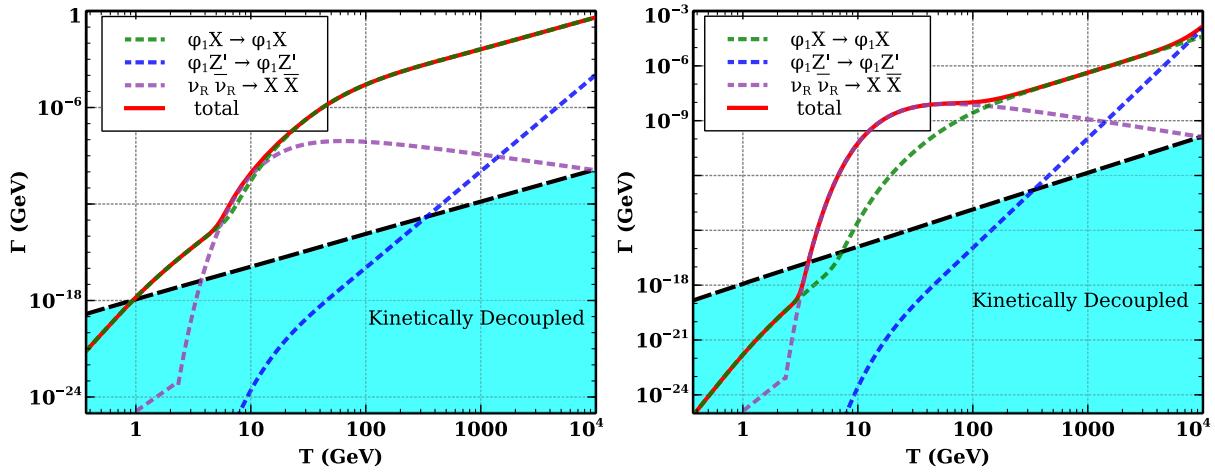

FIG. 7. Interaction rate as a function of temperature for processes responsible for keeping dark sector in equilibrium with the SM bath. The benchmark parameters chosen are $\lambda_{H\phi_1} = 10^{-2}$ (left panel), 10^{-4} (right panel), $m_{\phi_1} = 100$ GeV, $m_{Z'} = 100$ GeV, $g_{BL} = 10^{-4}$.

To track the evolution of dark sector, one has solve the Boltzmann equation in terms of comoving number densities Y_{ϕ_1} and Y_ψ. Using the approximation $\frac{Y_i}{Y} \approx \frac{Y_i^{\rm eq}}{Y^{\rm eq}}$ $(i = \phi_1, \psi)$, with $Y = Y_{\phi_1} + Y_\psi$, we can write a single Boltzmann equation as

$$\frac{dY}{dx} = \frac{1}{2}\frac{\beta s}{\mathcal{H}x}\langle\sigma v\rangle_{\rm eff}((Y^{\rm eq})^2 - Y^2), \tag{19}$$

where

$$\langle\sigma v\rangle_{\rm eff} = \frac{(Y_{\phi_1}^{eq})^2\langle\sigma v\rangle_{\phi_1\phi_1^\dagger\to X\bar{X},\ \nu_R\bar{\nu}_R,Z'Z'} + (Y_\psi^{eq})^2\langle\sigma v\rangle_{\psi\bar{\psi}\to\nu_R\bar{\nu}_R}}{(Y_{\phi_1}^{eq} + Y_\psi^{eq})^2}. \tag{20}$$

The equation (19) can be solved numerically from a sufficiently high temperature to the decoupling temperature, $T_{\rm dec}$. If the Yukawa coupling y_{ϕ_1} is large enough, even after $T < T_{\rm dec}$, the dark sector particles ϕ_1, ψ and ν_R can be in dark sector equilibrium among themselves. We can track the dark sector temperature $T_{\nu_R}(\equiv T_{\rm DS})$ by solving the following equation.

$$\frac{d\xi}{dx} = \frac{1}{x}\left(-\frac{1}{2}\frac{\beta x^4 s^2}{4\alpha\xi^3 H m_{\phi_1}^4}\langle E\sigma v\rangle_{\rm eff}((Y^{\rm eq})^2 - Y^2) - (\beta - 1)\xi\right), \tag{21}$$

where

$$\langle E\sigma v\rangle_{\rm eff} = \frac{(Y_{\nu_R}^{\rm eq})^2\langle E\sigma v\rangle_{\nu_R\bar{\nu}_R\to\psi\bar{\psi}} + (Y_{\nu_R}^{\rm eq})^2\langle E\sigma v\rangle_{\nu_R\bar{\nu}_R\to\phi_1\phi_1^\dagger}}{(Y_{\phi_1}^{\rm eq} + Y_\psi^{\rm eq})^2}, \tag{22}$$

and ξ is the ratio of dark sector temperature to that of the SM bath, $\frac{T_{\nu_R}}{T}$ and $\alpha = 6 \times \frac{7}{8}\frac{\pi^2}{30}$. After decoupling, $\langle\sigma v\rangle_{\rm eff}$ in Eq. (19) can depend upon both x as well as ξ. We solve Eq. (19) and Eq. (21) simultaneously from $T = T_{\rm dec}$ to the onset of the BBN era namely, $T \sim 10$ MeV and estimate the corresponding DM relic and $\Delta N_{\rm eff}$. Figure 8 shows the evolution of T_{ν_R} for different benchmark parameters. Different T_{ν_R} can lead to changes in $\Delta N_{\rm eff}$. The first term on the right-hand side (rhs) of Eq. (21) is a positive term as $Y \geq Y^{\rm eq}$ for $T < T_{\rm dec}$. Thus, this term indicates the increase in T_{ν_R} over T due to annihilation of heavy dark sector particles ϕ_1 and ψ into ν_R. On the other hand, the second term on the rhs of the same equation indicates the decrease in T_{ν_R} over T due to changes in entropy degrees of freedom g_*^s. The combined effects of these two terms can be seen in Fig. 8. For an analytical description of the behavior of the plots shown in Fig. 8, please refer to appendix D.

The left panel plot in Fig. 8 shows the variation of ξ^4 with respect to bath temperature T for different choices of $m_{Z'}$. The rest of the parameter are kept fixed as shown in the plot. Increasing $m_{Z'}$ gives a higher decoupling temperature, $T_{\rm dec}$. As long as $T_{\rm dec} \lesssim m_{\phi_1}$, a higher decoupling temperature leads to a larger conversion of ϕ_1 and ψ to ν_R resulting in a larger $\frac{T_{\nu_R}}{T}$. Another way to understand it is from entropy conservation (see appendix D). For a higher $T_{\rm dec}$, we have a larger dark sector entropy degrees of freedom $g_*^{s,\rm DS}$ resulting in a larger $\frac{T_{\nu_R}}{T}$. From an analytical estimation, we get a maximum value of ξ^4 to be 2.6 provided g_*^s remains same from the epoch of dark sector decoupling to DM freeze-out, as shown in appendix D. This is consistent with the numerical results shown in left panel of Fig. 8. The reason why maximum value of ξ^4 has not reached 2.6 in the figure is that g_*^s changes from the period of kinetic decoupling of dark sector to DM freeze-out. The middle panel plot shows the results for different values of dark

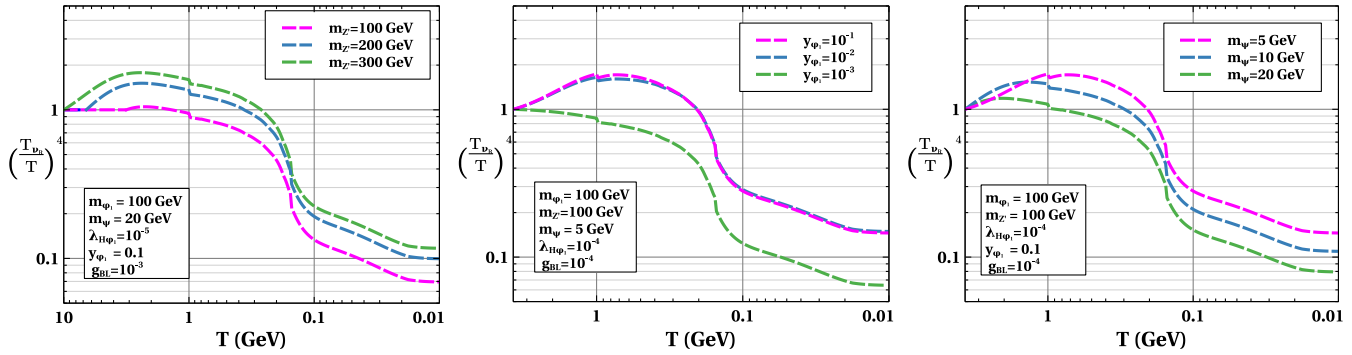

FIG. 8. Evolution of dark sector temperature after its decoupling from SM bath ($T < T_{\rm dec}$) for different values of $m_{Z'}$ (left panel), dark sector Yukawa coupling y_{ϕ_1} (middle panel) and dark matter mass m_ψ (right panel). The rest of the parameters are kept fixed and are shown in respective plots.

sector Yukawa coupling. As the dark sector Yukawa coupling does not affect the DM-SM decoupling temperature, so all the colored lines correspond to the same decoupling temperature. For a larger Yukawa coupling, conversion of ϕ_1 and ψ to ν_R is possible and as a result, temperature of ν_R with respect to SM bath increases. For the green line in the middle panel plot of Fig. 8, the dark sector freeze-out occurs before $T_{\rm dec}$ due to small Yukawa coupling. Hence the first term on the rhs of Eq. (21) ceases and due to the second term, the ratio $\frac{T_{\nu_R}}{T}$ decreases. To see the effect of m_ψ, in the right panel plot, we vary m_ψ keeping the other parameter constant. For a smaller m_ψ, freeze-out occurs late, hence we get a higher $\frac{T_{\nu_R}}{T}$ ratio.

To see the complete picture in WIMP dark matter scenario, we perform a numerical scan by varying the following parameters as

$$50\ \text{GeV} < m_{\phi_1} < 150\ \text{GeV}, \quad 100\ \text{GeV} < m_{Z'} < 500\ \text{GeV},$$
$$10\ \text{GeV} < m_\psi < 100\ \text{GeV}, \quad 10^{-5} < \lambda_{H\phi_1} < 10^{-2},$$
$$10^{-5} < g_{BL} < 10^{-3}, \quad 0.2 < y_{\phi_1} < 0.3. \tag{23}$$

The corresponding results are shown in Fig. 9 with y-axis representing $\Delta N_{\rm eff}$ whereas x-axis showing the mass of ϕ_1. The relevant parameters m_ψ, $m_{Z'}$ and g_{BL} are shown in color bars of left, middle, and right panel plots respectively of Fig. 9. All the points shown in this figure satisfy the requirements of correct WIMP DM relic abundance. The magenta shaded region denotes the region excluded by Planck 2018 bounds at 2σ CL while the gray shaded region remains within the reach of future experiments like CMB-S4. From the left panel plot, we can see that for some points with dark matter mass $m_\psi \lesssim 50$ GeV are already excluded by Planck 2018 data at 2σ CL. Similarly, from the middle and right panel plots, we get some points having $m_{Z'}$ between 100 GeV and 500 GeV and g_{BL} between 10^{-3} and 10^{-5} GeV, that are already excluded. All the others points in these plots can be probed in the future CMB experiments like CMB-S4 keeping the detection prospects promising.

As we have discussed above, the kinetic decoupling of the dark sector (ϕ, ψ and ν_R) from its bath is determined by both the Higgs-portal coupling and B-L gauge coupling. After the kinetic decoupling, due to large Yukawa coupling,

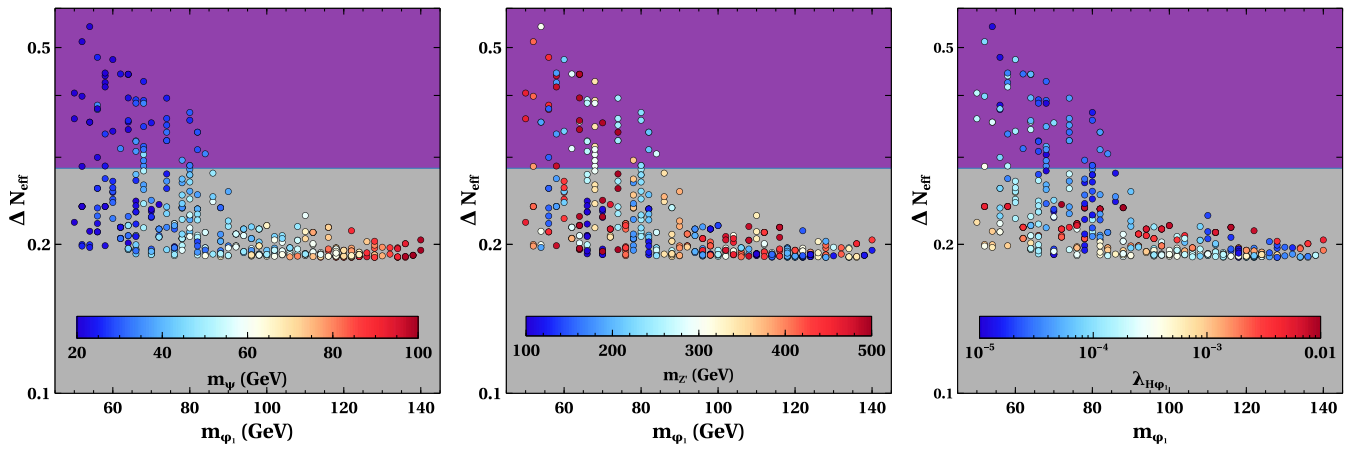

FIG. 9. Scan plot showing $\Delta N_{\rm eff}$ vs m_{ϕ_1} for different dark matter mass m_ψ and different $m_{Z'}$ and g_{BL}.

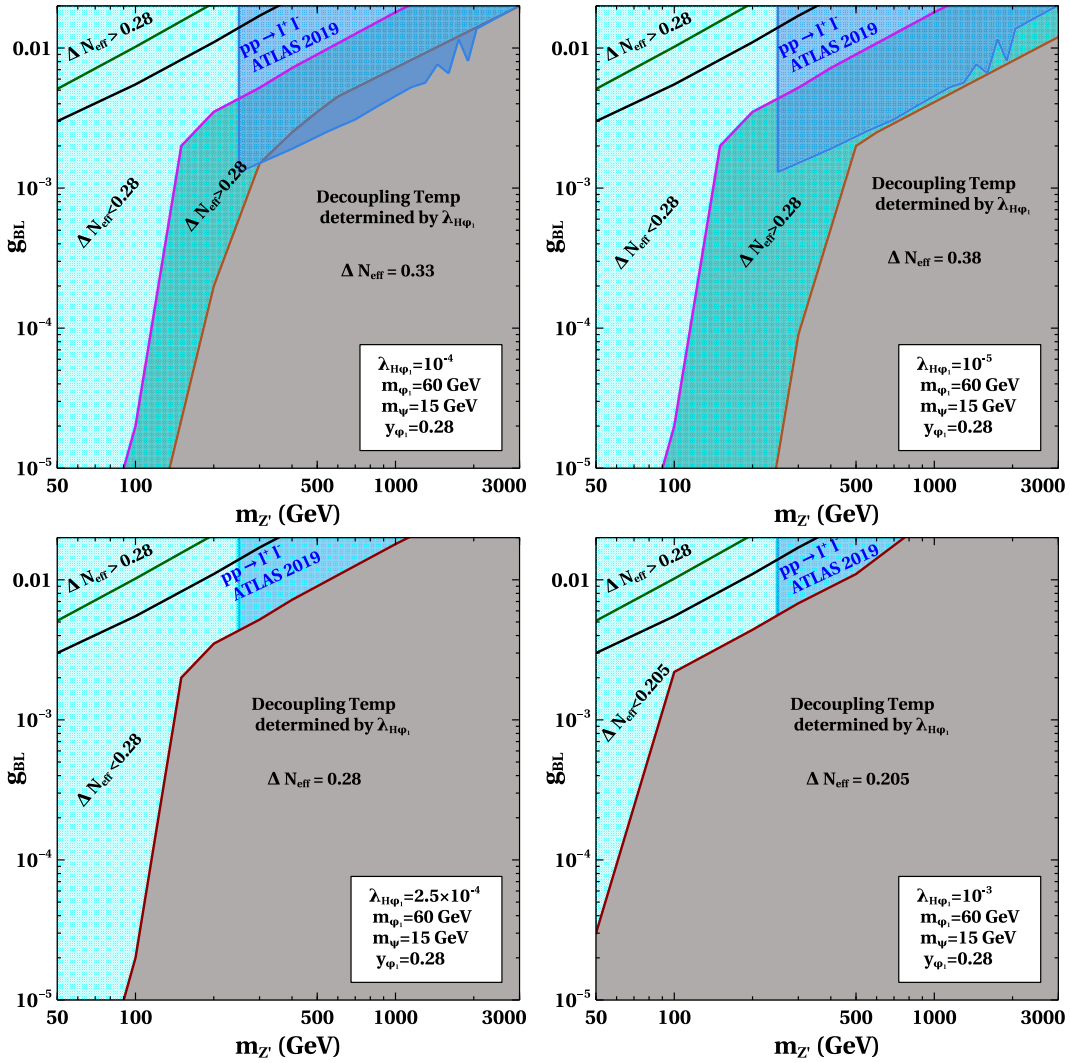

FIG. 10. Bound on $m_{Z'}$ vs g_{BL} for the WIMP scenario with different values of $\lambda_{H\phi_1}$. The solid black line separates regime 1 (below the solid black line) and regime 2 (above the solid black line). In all the plots, $m_{\phi_1} = 60$ GeV, $m_\psi = 15$ GeV, $y_{\phi_1} = 0.28$.

dark sector maintain a dark equilibrium. An increase in $\lambda_{H\phi_1}$ coupling or g_{BL} coupling keeps the dark sector in bath for longer. Increasing the g_{BL} coupling to a very high value gives us a scenario where the dark matter freezes out before the decoupling of ν_R. In this case, we do not have a separate dark sector evolution different from the SM bath. Hence, we have two regimes namely, regime 1: DM freezes out when $\xi_{\rm fo} \neq 1$ (i.e., separate dark sector); regime 2: DM freezes out when $\xi_{\rm fo} = 1$ (no separate dark sector). Depending upon whether kinetic decoupling temperature is determined by gauged B-L coupling (subcase 1) or Higgs-poral coupling (subcase 2) we can have two further subcases.

In the plots shown in Fig. 10, we show the parameter space in $m_{Z'}$ versus g_{BL} plane for WIMP type DM. Each of these plots correspond to a fixed value of $\lambda_{H\phi_1}$. The other parameters fixed in all the plots are, $m_{\phi_1} = 60$ GeV, $m_\psi = 15$ GeV, $y_{\phi_1} = 0.28$. The solid black line separates regime 1 (upper left triangular region) from regime 2. The solid brown line separates the regime where kinetic decoupling temperature is determined by Higgs portal coupling from the one where it is determined by the gauge portal coupling. In the gray colored region below the solid brown line, g_{BL} and $m_{Z'}$ have no role in the kinetic decoupling of dark sector. In the upper panel plots, the region below the magenta line is where we have $\Delta N_{\rm eff} > 0.28$, disfavored by Planck 2018 limits. In the gray colored region, due to constant decoupling temperature, we have constant $\Delta N_{\rm eff}$. Due to smaller Higgs-portal coupling in the upper right panel plot compared to the upper left one, the gray colored region shrinks. In the lower left panel plot, we increase the Higgs-portal coupling compared to upper left panel plot to 2.5×10^{-4}. For this particular choice of $\lambda_{H\phi_1}$, the region between the black and brown line has $\Delta N_{\rm eff} < 0.28$ and the region below the brown line has $\Delta N_{\rm eff} = 0.28$, which is the maximum

allowed value from Planck 2018 limits. In the lower right panel plot, $\lambda_{H\phi_1}$ is increased even further to 10^{-3} giving $\Delta N_{\rm eff} < 0.28$ in the whole regime 1. For regime 2, as DM freezes out before RHN decoupling, the bound from $\Delta N_{\rm eff}$ (denoted by region above the green line) is same as the bound shown in Fig. 1. The entire parameter space shown in these plots satisfy the criteria of DM relic abundance. This is because DM abundance has very weak dependence on the kinetic decoupling temperature. For the WIMP type DM scenario, we also check the constraints from direct detection and find them to be very weak due to radiative suppression. The details are given in appendix E.

V. CONCLUSION

We have studied a possible UV completion of the light Dirac neutrino portal dark matter scenario. In such a scenario, right chiral parts of light sub-eV Dirac neutrinos act like a portal between dark and visible sectors responsible for the production of dark matter. A gauged $U(1)_{B-L}$ symmetry provides one possible UV completion by naturally accommodating right chiral parts of neutrinos from anomaly cancellation requirements while also preventing direct coupling of DM, a gauge singlet Dirac fermion with the SM required for its stability. Keeping $U(1)_{B-L}$ symmetry breaking scale upto a few TeV ballpark, we study the details of dark matter production together with additional relativistic degrees of freedom $\Delta N_{\rm eff}$ brought in by right chiral parts of light Dirac neutrinos. While the chosen values of $U(1)_{B-L}$ gauge couplings ensures a nonzero thermal contribution to $\Delta N_{\rm eff}$, DM production can be either purely thermal or nonthermal depending upon the light Dirac neutrino portal Yukawa coupling. Although dark matter does not face stringent direct detection bounds due to loop-suppressed couplings with the SM quarks and charged leptons, the parameter space can be tightly constrained from other constraints related to structure formation, CMB constraints on $\Delta N_{\rm eff}$, collider constraints on $U(1)_{B-L}$ gauge bosons. We show interesting correlations in the parameter space from simultaneous requirement of correct DM phenomenology and $\Delta N_{\rm eff}$ indicating the region within reach of future CMB experiments.

ACKNOWLEDGMENTS

The work of D. B. is supported by the Science and Engineering Research Board (SERB), Government of India Grant No. MTR/2022/000575. N. D. would like to thank Anirban Biswas, Dibyendu Nanda, Pritam Das, Sahabub Jahedi, and Suruj Jyoti Das for useful discussions. The work of N. D. is supported by the Ministry of Education, Government of India via the Prime Minister's Research Fellowship (PMRF) December 2021 scheme.

APPENDIX A: ANOMALY CANCELLATION IN GAUGED $B-L$ MODEL

$U(1)_{B-L}$ gauge symmetry with only the SM fermions is not anomaly free. This is because the triangle anomalies for both $U(1)^3_{B-L}$ and the mixed $U(1)_{B-L}-(\text{gravity})^2$ diagrams are nonvanishing. These triangle anomalies for the SM fermion content are given as

$$\begin{aligned}\mathcal{A}_1[U(1)^3_{B-L}] &= \mathcal{A}_1^{\rm SM}[U(1)^3_{B-L}] = -3,\\ \mathcal{A}_2[(\text{gravity})^2\times U(1)_{B-L}] &= \mathcal{A}_2^{\rm SM}[(\text{gravity})^2\\ &\quad\times U(1)_{B-L}] = -3.\end{aligned} \tag{A1}$$

If three right-handed neutrinos are added to the model, they contribute $\mathcal{A}_1^{\rm New}[U(1)^3_{B-L}] = 3, \mathcal{A}_2^{\rm New}[(\text{gravity})^2\times U(1)_{B-L}] = 3$ leading to vanishing total of triangle anomalies. This is the most natural and economical $U(1)_{B-L}$ model studied extensively in the literature. However, there exist nonminimal ways of constructing anomaly free versions of $U(1)_{B-L}$ model. For example, it has been known for a few years that three right-handed neutrinos with $B-L$ charges $5,-4,-4$ can also give rise to vanishing triangle anomalies [70] as follows.

$$\begin{aligned}\mathcal{A}_1[U(1)^3_{B-L}] &= \mathcal{A}_1^{\rm SM}[U(1)^3_{B-L}] + \mathcal{A}_1^{\rm New}[U(1)^3_{B-L}] = -3+[-5^3-(-4)^3-(-4)^3] = 0,\\ \mathcal{A}_2[(\text{gravity})^2\times U(1)_{B-L}] &= \mathcal{A}_2^{\rm SM}[(\text{gravity})^2\times U(1)_{B-L}] + \mathcal{A}_2^{\rm New}[(\text{gravity})^2\times U(1)_{B-L}],\\ &= -3+[-5-(-4)-(-4)] = 0.\end{aligned} \tag{A2}$$

Another solution to the anomaly cancellation conditions with irrational $B-L$ charges of new fermions was proposed by the authors of [71] where both DM and neutrino mass can have a common origin through radiative linear seesaw. Very recently, another anomaly free $U(1)_{B-L}$ framework was proposed where the additional right-handed fermions possess more exotic $B-L$ charges namely, $-4/3,-1/3,-2/3,-2/3$ [72]. These four chiral fermions constitute two Dirac fermion mass eigenstates, the lighter of which becomes the DM candidate having either thermal [72] or nonthermal origins [73]. The light neutrino mass in this model arises from type II seesaw mechanism with the new chiral fermions playing no role in it. In [74], such chiral fermions with fractional charges were also responsible for generating light neutrino masses at one loop level. In the recent work on $U(1)_{B-L}$ gauge symmetry with two

component DM [75], the authors considered two right-handed neutrinos with $B-L$ number -1 each so that the model still remains anomalous. The remaining anomalies were canceled by four chiral fermions with fractional $B-L$ charges leading to two Dirac fermion mass eigenstates both of which are stable and hence DM candidates. In [76], type III seesaw was implemented in in $U(1)_{B-L}$ model while introducing additional chiral fermions to keep the model anomaly free. Appropriate choice of chiral fermions also leads to multicomponent DM in such $U(1)_{B-L}$ symmetric type III seesaw scenario.

While it is possible to study Dirac neutrino portal DM in gauged $U(1)_{B-L}$ frameworks with different anomaly free combinations of chiral fermions, it will require additional scalar fields in order to be consistent with the desired DM phenomenology and nonzero Dirac neutrino mass. For example, if we consider three right-handed neutrinos with $B-L$ charges $5,-4,-4$, we will require two additional Higgs doublets of $U(1)_{B-L}$ charge 6,3 respectively in order to generate Dirac neutrino masses at tree level. Two singlet scalars $\phi_{1,2}$ and DM ψ, similar to our model, can be incorporated to generate the Dirac neutrino portal of DM and break $U(1)_{B-L}$ symmetry spontaneously. Similar non-minimal scalar content will be required for other chiral fermions mentioned above. While the calculations will be more involved due to more particles, the generic conclusions reached in our work should not change significantly.

APPENDIX B: CALCULATION OF FSL

The free-streaming length (FSL) can be quantified as [59]

$$\lambda_{\rm FSL}=\int_{t_{\rm prod}}^{t_{\rm eq}}\frac{\langle v\rangle}{a}dt=\int_{T_{\rm prod}}^{T_{\rm eq}}\frac{\langle v(T)\rangle}{a(T)}\frac{dt}{dT}dT. \tag{B1}$$

Here $t_{\rm prod}$ ($T_{\rm prod}$) is the time (temperature) when maximum production of dark matter occurs. $t_{\rm eq}$ ($T_{\rm eq}$) is the time (temperature) of matter-radiation equality after which the structure formation starts. In terms of distribution function $f_\psi(q_1,T)$, the average velocity $\langle v(T)\rangle$ can be written as

$$\langle v(T)\rangle=\frac{\int\frac{q_1}{E_1}\frac{d^3q_1}{(2\pi)^3}f_\psi(q_1,T)}{\int\frac{d^3q_1}{(2\pi)^3}f_\psi(q_1,T)}. \tag{B2}$$

Here, q_1 and E_1 denotes the momentum and energy of dark matter respectively. To calculate the distribution function $f_\psi(q_1,T)$, it is convenient to change these variables to r and ξ_ψ given by

$$r=\frac{m_0}{T},\qquad \xi_\psi=\left(\frac{g_*^s(T_0)}{g_*^s(T)}\right)^{1/3}\frac{q_1}{T}, \tag{B3}$$

where m_0 and T_0 is some reference mass and temperature, respectively. For calculating $f_\psi(q_1,T)$, one also needs to calculate the distribution function of ϕ_1, $f_{\phi_1}(p,T)$.

For the process $\phi_1(p_1)\to\psi(q_1)+\nu_R(q_2)$, the Boltzmann equation for the distribution function of ψ can be written as

$$\frac{\partial f_\psi}{\partial t}-\mathcal{H}q_1\frac{\partial f_\psi}{\partial q_1}=\frac{1}{16\pi E_{q_1}q_1}\int_{p_1^{\rm min}}^{p_1^{\rm max}}\frac{p_1dp_1}{E_{p_1}}|\mathcal{M}|^2_{\phi\to\bar\nu_R\psi}f_{\phi_1}(p_1). \tag{B4}$$

The expressions for $p_1^{\rm max}$ and $p_1^{\rm min}$ for $m_{\phi_1}\gg m_\psi$ are

$$p_1^{\rm min}\simeq\frac{m_{\phi_1}^2}{2m_\psi^2}\left(-q_1+\sqrt{q_1^2-4\frac{m_\psi^2}{m_{\phi_1}^2}q_1^2+m_\psi^2}\right), \tag{B5}$$

$$p_1^{\rm max}\simeq\frac{m_{\phi_1}^2}{2m_\psi^2}\left(q_1+\sqrt{q_1^2-4\frac{m_\psi^2}{m_{\phi_1}^2}q_1^2+m_\psi^2}\right). \tag{B6}$$

The distribution function for ϕ_1 after its freeze-out can be obtained from

$$\begin{aligned}\frac{\partial f_{\phi_1}}{\partial t}-\mathcal{H}p_1\frac{\partial f_{\phi_1}}{\partial p_1}&=-\frac{1}{2E_{p_1}}\int\frac{d^3q_1}{2E_{q_1}(2\pi)^3}\frac{d^3q_2}{2E_{q_2}(2\pi)^3}\\&\quad\times(2\pi)^4\delta^4(P_1-Q_1-Q_2)\\&\quad\times|\mathcal{M}|^2_{\phi_1\to\psi\bar\nu_R}f_{\phi_1}(p_1)\\&=-f_{\phi_1}\frac{m_{\phi_1}}{\sqrt{p_1^2+m_{\phi_1}^2}}\Gamma_{\phi_1\to\psi\bar\nu_R}.\end{aligned} \tag{B7}$$

Here P_1, Q_1, and Q_2 are the four momenta corresponding to ϕ_1, ψ, and ν_R, respectively. With these above equations and using the transformation $r=\frac{m_0}{T}$, $\xi_\psi=(\frac{g_*^s(T_0)}{g_*^s(T)})^{1/3}\frac{q_1}{T}$, we obtain the distribution function $f_\psi(\xi_\psi,r)$ [6,73,77]. With these, the average velocity of DM and free-streaming length can be reexpressed in terms of new variables as

$$\langle v(r)\rangle=\frac{\mathcal{A}(r)}{\int\xi_\psi^2f_\psi(\xi_\psi,r)d\xi_\psi}\times\int\frac{\xi_\psi^3f_\psi(\xi_\psi,r)d\xi_\psi}{\sqrt{(\mathcal{A}(r)\xi_\psi)^2+(\frac{r}{m_0}m_\psi)^2}} \tag{B8}$$

$$\lambda_{\rm FSL}=\left(\frac{11}{43}\right)^{1/3}r_0\int_{r_{\rm prod}}^{r_{\rm eq}}\langle v(r)\rangle g_s^{1/3}\frac{\beta}{\mathcal{H}(r)}\frac{dr}{r^2}, \tag{B9}$$

where $\mathcal{A}(r)=(\frac{g_*^s(m_0/r)}{g_*^s(m_0/T_0)})^{1/3}$.

APPENDIX C: CALCULATION OF LHC BOUND ON $g_{BL}-m_{Z'}$ PLANE

We evaluate the constraint on $U(1)_{B-L}$ gauge coupling g_{BL} from dilepton channel: $pp\to Z'\to l^+l^-$. Using the

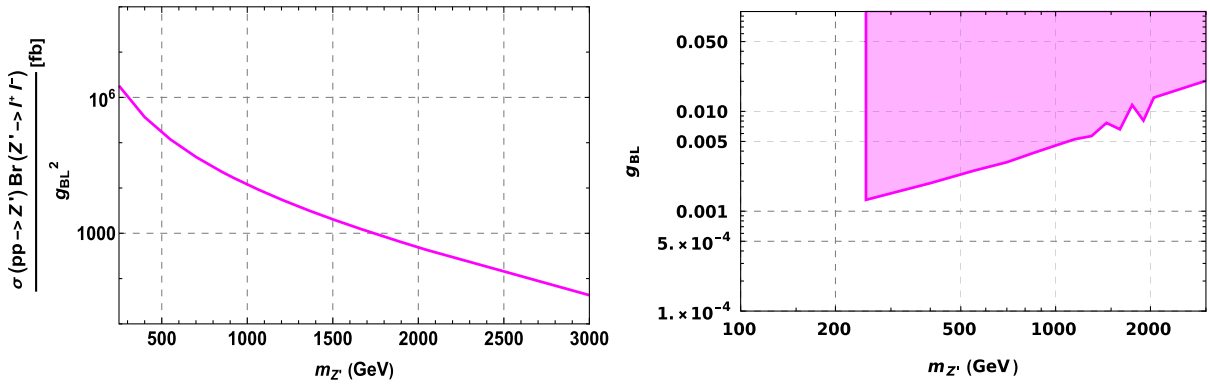

FIG. 11. Left panel: $\frac{\sigma(pp\to Z')\mathrm{BR}(Z'\to l^-l^+)}{g_{BL}^2}$ vs $m_{Z'}$. Right panel: bound on g_{BL} vs $m_{Z'}$ plane.

narrow-width approximation, the cross section $pp \to Z'$ can be written as

$$\sigma(pp \to Z') = 2\sum_{q,\bar{q}} \int dx \int dy\, f_q(x,Q) f_{\bar{q}}(x,Q)\hat{\sigma}(\hat{s}), \tag{C1}$$

where $\hat{s} = xys$ with f_q, $f_{\bar{q}}$ being the parton distribution functions for quarks and antiquark, respectively. The narrow-width approximation cross section $\hat{\sigma}(\hat{s})$ is given as

$$\hat{\sigma}(\hat{s}) = \frac{4\pi^2}{3}\frac{\Gamma(Z' \to q\bar{q})}{m_{Z'}}\delta(\hat{s} - m_{Z'}^2). \tag{C2}$$

We use the package CALCHEP for the computation of $\sigma(pp \to Z')$ where CTEQ6L is used for parton distribution functions.

In our model, apart from quarks and leptons, three ν_Rs and two scalars ϕ_1 and ϕ_2 are charged under $U(1)_{B-L}$. The decay of Z' to both the BSM scalars ϕ_1 and ϕ_2 is not possible due to kinematic restrictions imposed. The decay width of Z' to quarks, charged leptons, SM neutrinos and ν_R can be written as

$$\begin{aligned}
\Gamma(Z' \to q\bar{q}) &\simeq 12 \times 3 \times \frac{1}{9}\frac{g_{BL}^2}{24\pi} m_{Z'} = 4 \times \frac{g_{BL}^2}{24\pi} m_{Z'} \\
\Gamma(Z' \to l^- l^+) &\simeq 6 \times \frac{g_{BL}^2}{24\pi} m_{Z'} \\
\Gamma(Z' \to \nu_L \bar{\nu}_L) &\simeq 3 \times \frac{g_{BL}^2}{24\pi} m_{Z'} \\
\Gamma(Z' \to \nu_R \bar{\nu}_R) &\simeq 3 \times \frac{g_{BL}^2}{24\pi} m_{Z'}
\end{aligned} \tag{C3}$$

respectively, assuming massless final states. With this, we can calculate the cross section $\sigma(pp \to Z' \to l^+l^-) \approx \sigma(pp \to Z')\mathrm{BR}(Z' \to l^-l^+)$ for particular values of $m_{Z'}$ and g_{BL}. As $\sigma(pp \to Z')$ is proportional to g_{BL}^2, we can normalize it by dividing with g_{BL}^2.

The left panel plot of Fig. 11 shows $\frac{\sigma(pp\to Z')\mathrm{BR}(Z'\to l^-l^+)}{g_{BL}^2}$ as a function of $m_{Z'}$ for our model. In the right panel plot, we show the bound on $U(1)_{B-L}$ gauge coupling for our model in magenta region. The bound is obtained by comparing the left plot with the final results from ATLAS collaboration of the LHC Run-2 with 139 fb^{-1} integrated luminosity.

APPENDIX D: ESTIMATION OF DARK SECTOR TEMPERATURE

Here we provide an estimation of dark sector temperature using the entropy conservation. Let us assume that $g_*^{s,\mathrm{DS}}$ and g_*^s are the effective number of relativistic degree of freedom of dark sector and standard model, respectively. At the epoch of decoupling of dark sector from the standard model bath, the scale factor is taken as a_{dec}. Using the conservation of entropy, we get

$$\begin{aligned}
g_{*,\mathrm{dec}}^s a_{\mathrm{dec}}^3 (T_{\mathrm{dec}})^3 &= g_{*,\mathrm{aft}}^s a_{\mathrm{aft}}^3 (T_{\mathrm{aft}})^3 \\
g_{*,\mathrm{dec}}^{s,\mathrm{DS}} a_{\mathrm{dec}}^3 (T_{\mathrm{dec}}^{\mathrm{DS}})^3 &= g_{*,\mathrm{aft}}^{s,\mathrm{DS}} a_{\mathrm{aft}}^3 (T_{\mathrm{aft}}^{\mathrm{DS}})^3,
\end{aligned} \tag{D1}$$

where a_{aft} denotes any period after decoupling and T^{DS} and T denote temperature of dark sector and SM bath, respectively. At the epoch of decoupling, both the dark sector and SM bath have same temperature, $T_{\mathrm{dec}} = T_{\mathrm{dec}}^{\mathrm{DS}}$. Hence, from the above equations, we get

$$\left(\frac{T_{\mathrm{aft}}^{\mathrm{DS}}}{T_{\mathrm{aft}}}\right)^4 = \left(\frac{g_{*,\mathrm{dec}}^{s,\mathrm{DS}}}{g_{*,\mathrm{aft}}^{s,\mathrm{DS}}}\frac{g_{*,\mathrm{aft}}^s}{g_{*,\mathrm{dec}}^s}\right)^{4/3}. \tag{D2}$$

For the situation where dark sector consists of ϕ_1, ψ and ν_R, we have $g_{*,\mathrm{dec}}^{s,\mathrm{DS}} = 2 + 6 \times \frac{7}{8} + 4 \times \frac{7}{8} = 10.75$. Taking a_{aft} to a period when both ϕ_1 and ψ annihilate or become nonrelativistic, we get $g_{*,\mathrm{aft}}^{s,\mathrm{DS}} = 6 \times \frac{7}{8} = 5.25$. If during this period, g_*^s remains constant, we get

$$\left(\frac{T_{\mathrm{aft}}^{\mathrm{DS}}}{T_{\mathrm{aft}}}\right)^4 = \xi^4 = \left(\frac{10.75}{5.25}\right)^{4/3} = 2.6. \tag{D3}$$

So, at maximum, we can expect a 2.6 times increase in dark sector temperature from the SM bath. The numerical results shown in Fig. 8 are consistent with this analytical estimation.

However, we can have a value of $g_{*,\mathrm{dec}}^{s,\mathrm{DS}} < 10.75$ at the epoch of decoupling. This is because before decoupling, some fraction of dark sector particles can become nonrelativistic. For example, let us consider $m_{\phi_1} = 60$ GeV, $m_\psi = 15$ GeV. Decoupling above $T \sim 60$ GeV gives $g_{*,\mathrm{dec}}^{s,\mathrm{DS}} \sim 10.75$ whereas decoupling after $T \sim 60$ GeV (e.g., 10 GeV) gives $g_{*,\mathrm{dec}}^{s,\mathrm{DS}} < 10.75$. This results in a smaller increase in dark sector temperature from SM bath. The same behavior can also been seen from Fig. 8.

APPENDIX E: DIRECT DETECTION OF WIMP TYPE DM

In this setup, dark matter ψ does not interact with the nucleus via tree level diagram. However, via one loop diagram, it can scatter off the nucleus. We get two diagrams, one where the mediator is SM Higgs and the other where the mediator is B-L gauged boson. For the Higgs mediated diagram, the relevant interaction vertices are $g_{\psi\bar{\psi}h}\psi\bar{\psi}h$ and $\frac{m_q}{v}q\bar{q}$. Here q represents the SM quarks. The effective interaction term for Higgs mediated diagram can be written as

$$\mathcal{L}_{\mathrm{eff}}^{h} = \frac{m_q}{v}\frac{1}{m_h^2} g_{\psi\bar{\psi}h}\psi\bar{\psi}q\bar{q}. \tag{E1}$$

Similarly for the Z' mediated diagram, the effective interaction term can be written as

$$\mathcal{L}_{\mathrm{eff}}^{Z'} = -\frac{g_{BL}}{3}\frac{1}{m_{Z'}^2} g_{\psi\bar{\psi}Z'}\psi\gamma^\mu\bar{\psi}q\gamma_\mu\bar{q}. \tag{E2}$$

The interaction vertices $g_{\psi\bar{\psi}h}$ and $g_{\psi\bar{\psi}Z'}$ for one loop diagram are calculated using Package-X [78] and their expressions are given as follows (for zero momentum transfer)[8]

[8]We consider only one of the two different one-loop diagrams to calculate the effective $g_{\psi\bar{\psi}Z'}$ vertex for simplicity.

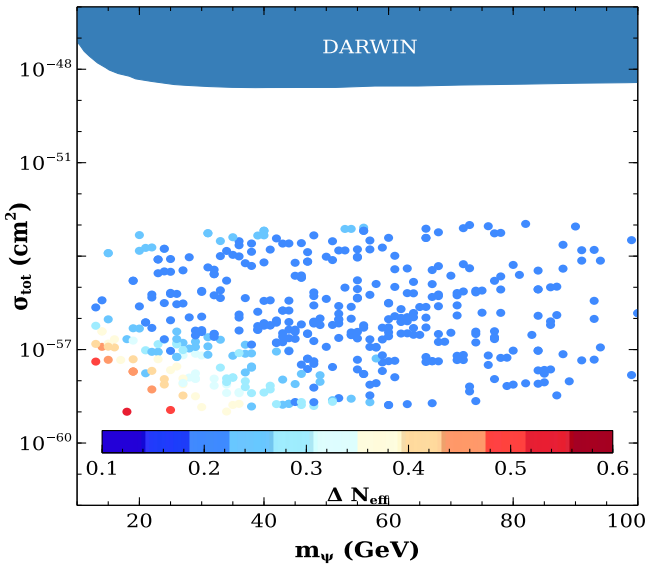

FIG. 12. The DM-nucleon cross section vs DM mass as a function of effective number of relativistic species. The blue color region shows the sensitivity of DARWIN experiment [82].

$$g_{\psi\bar{\psi}h} = \frac{i}{16\pi^2} y_{\phi_1}^2 \lambda_{H\phi_1} v \frac{1}{m_\psi}\left[1 + \left(\frac{m_{\phi_1}^2}{m_\psi^2} - 1\right)\ln\left(1 - \frac{m_\psi^2}{m_{\phi_1}^2}\right)\right]$$

$$g_{\psi\bar{\psi}Z'} = \frac{i}{16\pi^2} y_{\phi_1}^2 g_{BL}\left[\frac{3}{2}\frac{m_{\phi_1}^2}{m_\psi^2} + \left(\frac{m_{\phi_1}^2}{m_\psi^2} - 1\right)\ln\left(1 - \frac{m_\psi^2}{m_{\phi_1}^2}\right)\left(\frac{3}{2}\frac{m_{\phi_1}^2}{m_\psi^2} + \frac{1}{2}\right)\right]. \tag{E3}$$

The total DM-nucleon cross section can be written as [79–81]

$$\sigma_{\mathrm{tot}} = \frac{1}{\pi}\frac{m_N^2 m_\psi^2}{(m_N + m_\psi)^2}\left[\frac{m_N}{v}\frac{1}{m_h^2} g_{\psi\bar{\psi}h} f_N + \frac{g_{BL}}{3}\frac{1}{m_{Z'}^2} g_{\psi\bar{\psi}Z'} f_{Z'}\right]^2, \tag{E4}$$

where $f_N \sim 0.3$, $f_{Z'} = 3$ and m_N is the nucleon mass. In Fig. 12, we show the DM-nucleon cross section as a function of m_ψ. To calculate the cross section, we take the values of different parameters same as for the resultant points we obtained in Fig. 9. All the points satisfy correct DM relic abundance and range of different parameters for these points are given by Eq. (23). We find that the total cross section is way below the direct detection limit.

[1] Particle Data Group Collaboration, Review of particle physics, Prog. Theor. Exp. Phys. **2020**, 083C01 (2020).
[2] Planck Collaboration, Planck 2018 results. VI. Cosmological parameters, arXiv:1807.06209.
[3] G. Arcadi, M. Dutra, P. Ghosh, M. Lindner, Y. Mambrini, M. Pierre, S. Profumo, and F. S. Queiroz, The waning of the WIMP? A review of models, searches, and constraints, Eur. Phys. J. C **78**, 203 (2018).
[4] N. Bernal, M. Heikinheimo, T. Tenkanen, K. Tuominen, and V. Vaskonen, The dawn of FIMP dark matter: A review of models and constraints, Int. J. Mod. Phys. A **32**, 1730023 (2017).
[5] A. Biswas, D. Borah, and D. Nanda, Light Dirac neutrino portal dark matter with observable ΔNeff, J. Cosmol. Astropart. Phys. 10 (2021) 002.
[6] A. Biswas, D. Borah, N. Das, and D. Nanda, Freeze-in dark matter via a light Dirac neutrino portal, Phys. Rev. D **107**, 015015 (2023).
[7] A. Falkowski, J. Juknevich, and J. Shelton, Dark matter through the neutrino portal, arXiv:0908.1790.
[8] V. Gonzalez Macias and J. Wudka, Effective theories for dark matter interactions and the neutrino portal paradigm, J. High Energy Phys. 07 (2015) 161.
[9] B. Batell, T. Han, and B. Shams Es Haghi, Indirect detection of neutrino portal dark matter, Phys. Rev. D **97**, 095020 (2018).
[10] B. Batell, T. Han, D. McKeen, and B. Shams Es Haghi, Thermal dark matter through the Dirac neutrino portal, Phys. Rev. D **97**, 075016 (2018).
[11] P. Bandyopadhyay, E. J. Chun, R. Mandal, and F. S. Queiroz, Scrutinizing right-handed neutrino portal dark matter with Yukawa effect, Phys. Lett. B **788**, 530 (2019).
[12] M. Chianese and S. F. King, The dark side of the littlest seesaw: Freeze-in, the two right-handed neutrino portal and leptogenesis-friendly fimpzillas, J. Cosmol. Astropart. Phys. 09 (2018) 027.
[13] M. Blennow, E. Fernandez-Martinez, A. Olivares-Del Campo, S. Pascoli, S. Rosauro-Alcaraz, and A. Titov, Neutrino portals to dark matter, Eur. Phys. J. C **79**, 555 (2019).
[14] J. Lamprea, E. Peinado, S. Smolenski, and J. Wudka, Strongly interacting neutrino portal dark matter, Phys. Rev. D **103**, 015017 (2021).
[15] M. Chianese, B. Fu, and S. F. King, Minimal Seesaw extension for neutrino mass and mixing, leptogenesis and dark matter: FIMPzillas through the right-handed neutrino portal, J. Cosmol. Astropart. Phys. 03 (2020) 030.
[16] P. Bandyopadhyay, E.,J. Chun, and R. Mandal, Feeble neutrino portal dark matter at neutrino detectors, J. Cosmol. Astropart. Phys. 08 (2020) 019.
[17] E. Hall, T. Konstandin, R. McGehee, and H. Murayama, Asymmetric matters from a dark first-order phase transition, Phys. Rev. D **107**, 055011 (2023).
[18] A. Berlin and N. Blinov, Thermal neutrino portal to sub-MeV dark matter, Phys. Rev. D **99**, 095030 (2019).
[19] Planck Collaboration, Planck 2018 results. VI. Cosmological parameters, Astron. Astrophys. **641**, A6 (2020).
[20] R. H. Cyburt, B. D. Fields, K. A. Olive, and T.-H. Yeh, Big bang nucleosynthesis: 2015, Rev. Mod. Phys. **88**, 015004 (2016).
[21] G. Mangano, G. Miele, S. Pastor, T. Pinto, O. Pisanti, and P. D. Serpico, Relic neutrino decoupling including flavor oscillations, Nucl. Phys. **B729**, 221 (2005).
[22] E. Grohs, G. M. Fuller, C. T. Kishimoto, M. W. Paris, and A. Vlasenko, Neutrino energy transport in weak decoupling and big bang nucleosynthesis, Phys. Rev. D **93**, 083522 (2016).
[23] P. F. de Salas and S. Pastor, Relic neutrino decoupling with flavour oscillations revisited, J. Cosmol. Astropart. Phys. 07 (2016) 051.
[24] M. Cielo, M. Escudero, G. Mangano, and O. Pisanti, Neff in the standard model at NLO is 3.043, Phys. Rev. D **108**, L121301 (2023).
[25] K. Abazajian *et al.*, CMB-S4 science case, reference design, and project plan, arXiv:1907.04473.
[26] K. N. Abazajian and J. Heeck, Observing Dirac neutrinos in the cosmic microwave background, Phys. Rev. D **100**, 075027 (2019).
[27] P. Fileviez Pérez, C. Murgui, and A. D. Plascencia, Neutrino-dark matter connections in gauge theories, Phys. Rev. D **100**, 035041 (2019).
[28] D. Nanda and D. Borah, Connecting light Dirac neutrinos to a multi-component dark matter scenario in gauged $B-L$ model, Eur. Phys. J. C **80**, 557 (2020).
[29] C. Han, M. López-Ibáñez, B. Peng, and J. M. Yang, Dirac dark matter in $U(1)_{B-L}$ with Stueckelberg mechanism, Nucl. Phys. **B959**, 115154 (2020).
[30] X. Luo, W. Rodejohann, and X.-J. Xu, Dirac neutrinos and $N_{\rm eff}$, J. Cosmol. Astropart. Phys. 06 (2020) 058.
[31] D. Borah, A. Dasgupta, C. Majumdar, and D. Nanda, Observing left-right symmetry in the cosmic microwave background, Phys. Rev. D **102**, 035025 (2020).
[32] P. Adshead, Y. Cui, A. J. Long, and M. Shamma, Unraveling the Dirac neutrino with cosmological and terrestrial detectors, Phys. Lett. B **823**, 136736 (2021).
[33] X. Luo, W. Rodejohann, and X.-J. Xu, Dirac neutrinos and $N_{\rm eff}$ II: The freeze-in case, J. Cosmol. Astropart. Phys. 03 (2021) 082.
[34] D. Mahanta and D. Borah, Low scale Dirac leptogenesis and dark matter with observable $\Delta N_{\rm eff}$, Eur. Phys. J. C **82**, 495 (2022).
[35] Y. Du and J.-H. Yu, Neutrino non-standard interactions meet precision measurements of $N_{\rm eff}$, J. High Energy Phys. 05 (2021) 058.
[36] D. Borah, S. Mahapatra, D. Nanda, and N. Sahu, Type II Dirac Seesaw with observable $\Delta N_{\rm eff}$ in the light of W-mass anomaly, Phys. Lett. B **833**, 137297 (2022).
[37] D. Borah, S. Jyoti Das, and N. Okada, Affleck-Dine cogenesis of baryon and dark matter, J. High Energy Phys. 05 (2023) 004.
[38] S.-P. Li, X.-Q. Li, X.-S. Yan, and Y.-D. Yang, Effective neutrino number shift from keV-vacuum neutrinophilic 2HDM, Chin. Phys. C **47**, 043109 (2023).
[39] A. Biswas, D. K. Ghosh, and D. Nanda, Concealing Dirac neutrinos from cosmic microwave background, J. Cosmol. Astropart. Phys. 10 (2022) 006.
[40] P. Adshead, P. Ralegankar, and J. Shelton, Dark radiation constraints on portal interactions with hidden sectors, J. Cosmol. Astropart. Phys. 09 (2022) 056.

[41] D. Borah, S. Mahapatra, D. Nanda, S. K. Sahoo, and N. Sahu, Singlet-doublet fermion dark matter with Dirac neutrino mass, $(g-2)_\mu$ and $\Delta N_{\rm eff}$, arXiv:2310.03721.
[42] D. Borah, P. Das, and D. Nanda, Observable $\Delta N_{\rm eff}$ in Dirac scotogenic model, Eur. Phys. J. C **84**, 140 (2024).
[43] N. Das, S. Jyoti Das, and D. Borah, Thermalized dark radiation in the presence of a PBH: ΔNeff and gravitational waves complementarity, Phys. Rev. D **108**, 095052 (2023).
[44] A. Davidson, B–L as the fourth color within an $\mathrm{SU}(2)_L \times \mathrm{U}(1)_R \times \mathrm{U}(1)$ model, Phys. Rev. D **20**, 776 (1979).
[45] R. N. Mohapatra and R. E. Marshak, Local B-L symmetry of electroweak interactions, Majorana neutrinos and neutron oscillations, Phys. Rev. Lett. **44**, 1316 (1980).
[46] R. E. Marshak and R. N. Mohapatra, Quark—lepton symmetry and B-L as the U(1) generator of the electroweak symmetry group, Phys. Lett. **91B**, 222 (1980).
[47] A. Masiero, J. F. Nieves, and T. Yanagida, B^-l violating proton decay and late cosmological baryon production, Phys. Lett. **116B**, 11 (1982).
[48] R. N. Mohapatra and G. Senjanovic, Spontaneous breaking of global B^-l symmetry and matter—antimatter oscillations in grand unified theories, Phys. Rev. D **27**, 254 (1983).
[49] W. Buchmuller, C. Greub, and P. Minkowski, Neutrino masses, neutral vector bosons and the scale of B-L breaking, Phys. Lett. B **267**, 395 (1991).
[50] M. Drewes *et al.*, A white paper on keV sterile neutrino dark matter, J. Cosmol. Astropart. Phys. 01 (2017) 025.
[51] R. A. C. Croft, D. H. Weinberg, M. Bolte, S. Burles, L. Hernquist, N. Katz *et al.*, Towards a precise measurement of matter clustering: Lyman-α forest data at redshifts 2-4, Astrophys. J. **581**, 20 (2002).
[52] T. S. Kim, M. Viel, M. G. Haehnelt, R. F. Carswell, and S. Cristiani, The power spectrum of the flux distribution in the Lyman-α forest of a large sample of uves QSO absorption spectra (LUQAS), Mon. Not. R. Astron. Soc. **347**, 355 (2004).
[53] M. Viel, J. Lesgourgues, M. G. Haehnelt, S. Matarrese, and A. Riotto, Constraining warm dark matter candidates including sterile neutrinos and light gravitinos with WMAP and the Lyman-alpha forest, Phys. Rev. D **71**, 063534 (2005).
[54] V. Iršič *et al.*, New Constraints on the free-streaming of warm dark matter from intermediate and small scale Lyman-α forest data, Phys. Rev. D **96**, 023522 (2017).
[55] J.-W. Hsueh, W. Enzi, S. Vegetti, M. Auger, C. D. Fassnacht, G. Despali, L. V. E Koopmans, and J. P. McKean, SHARP—VII. New constraints on the dark matter free-streaming properties and substructure abundance from gravitationally lensed quasars, Mon. Not. R. Astron. Soc. **492**, 3047 (2020).
[56] S. Colombi, S. Dodelson, and L. M. Widrow, Large scale structure tests of warm dark matter, Astrophys. J. **458**, 1 (1996).
[57] A. Boyarsky, J. Lesgourgues, O. Ruchayskiy, and M. Viel, Lyman-α constraints on warm and on warm-plus-cold dark matter models, J. Cosmol. Astropart. Phys. 05 (2009) 012.
[58] H. J. de Vega and N. G. Sanchez, Model independent analysis of dark matter points to a particle mass at the keV scale, Mon. Not. R. Astron. Soc. **404**, 885 (2010).
[59] A. Schneider, R. E. Smith, A. V. Maccio, and B. Moore, Nonlinear evolution of cosmological structures in warm dark matter models, Mon. Not. R. Astron. Soc. **424**, 684 (2012).
[60] A. Merle, V. Niro, and D. Schmidt, New production mechanism for keV sterile neutrino dark matter by decays of frozen-in scalars, J. Cosmol. Astropart. Phys. 03 (2014) 028.
[61] Q. Decant, J. Heisig, D. C. Hooper, and L. Lopez-Honorez, Lyman-α constraints on freeze-in and superWIMPs, J. Cosmol. Astropart. Phys. 03 (2022) 041.
[62] G. Ballesteros, M. A. G. Garcia, and M. Pierre, How warm are non-thermal relics? Lyman-α bounds on out-of-equilibrium dark matter, J. Cosmol. Astropart. Phys. 03 (2021) 101.
[63] ATLAS Collaboration, Search for high-mass dilepton resonances using 139 fb^{-1} of pp collision data collected at $\sqrt{s} = 13$ TeV with the ATLAS detector, Phys. Lett. B **796**, 68 (2019).
[64] ATLAS Collaboration, Search for new high-mass phenomena in the dilepton final state using 36 fb^{-1} of proton-proton collision data at $\sqrt{s} = 13$ TeV with the ATLAS detector, J. High Energy Phys. 10 (2017) 182.
[65] CMS Collaboration, Search for high-mass resonances in dilepton final states in proton-proton collisions at $\sqrt{s} = 13$ TeV, J. High Energy Phys. 06 (2018) 120.
[66] M. Carena, A. Daleo, B. A. Dobrescu, and T. M. P. Tait, Z' gauge bosons at the Tevatron, Phys. Rev. D **70**, 093009 (2004).
[67] G. Cacciapaglia, C. Csaki, G. Marandella, and A. Strumia, The minimal set of electroweak precision parameters, Phys. Rev. D **74**, 033011 (2006).
[68] P. Gondolo, J. Hisano, and K. Kadota, The effect of quark interactions on dark matter kinetic decoupling and the mass of the smallest dark halos, Phys. Rev. D **86**, 083523 (2012).
[69] J. Heeck, Unbroken B—L symmetry, Phys. Lett. B **739**, 256 (2014).
[70] J. C. Montero and V. Pleitez, Gauging U(1) symmetries and the number of right-handed neutrinos, Phys. Lett. B **675**, 64 (2009).
[71] W. Wang and Z.-L. Han, Radiative linear seesaw model, dark matter, and $U(1)_{B-L}$, Phys. Rev. D **92**, 095001 (2015).
[72] S. Patra, W. Rodejohann, and C. E. Yaguna, A new B ? L model without right-handed neutrinos, J. High Energy Phys. 09 (2016) 076.
[73] A. Biswas and A. Gupta, Calculation of momentum distribution function of a non-thermal fermionic dark matter, J. Cosmol. Astropart. Phys. 03 (2017) 033.
[74] D. Nanda and D. Borah, Common origin of neutrino mass and dark matter from anomaly cancellation requirements of a $U(1)_{B-L}$ model, Phys. Rev. D **96**, 115014 (2017).
[75] N. Bernal, D. Restrepo, C. Yaguna, and O. Zapata, Two-component dark matter and a massless neutrino in a new $B-L$ model, Phys. Rev. D **99**, 015038 (2019).
[76] A. Biswas, D. Borah, and D. Nanda, Type III Seesaw for neutrino masses in $U(1)_{B-L}$ model with multi-component dark matter, J. High Energy Phys. 12 (2019) 109.

[77] J. König, A. Merle, and M. Totzauer, keV sterile neutrino dark matter from singlet scalar decays: The most general case, J. Cosmol. Astropart. Phys. 11 (2016) 038.

[78] H. H. Patel, Package-X 2.0: A Mathematica package for the analytic calculation of one-loop integrals, Comput. Phys. Commun. **218**, 66 (2017).

[79] A. Biswas, S. Choubey, and S. Khan, Galactic gamma ray excess and dark matter phenomenology in a $U(1)_{B-L}$ model, J. High Energy Phys. 08 (2016) 114.

[80] S. Bhattacharya, J. Lahiri, and D. Pradhan, Detection possibility of a pseudo-FIMP in presence of a thermal WIMP, arXiv:2212.14846.

[81] G. Jungman, M. Kamionkowski, and K. Griest, Supersymmetric dark matter, Phys. Rep. **267**, 195 (1996).

[82] DARWIN Collaboration, DARWIN: Towards the ultimate dark matter detector, J. Cosmol. Astropart. Phys. 11 (2016) 017.